Linear stability of viscous supersonic plane Couette flow

Sean Hu and Xiaolin Zhong
Mechanical and Aerospace Engineering Department, University of California, Los Angeles, California 90095

(Received 30 April 1997; accepted 5 November 1997)

The linear stability of viscous compressible plane Couette flow is not well understood even though the stability of incompressible Couette flow has been studied extensively and has been shown to be stable to linear disturbances. In this paper, the viscous linear stability of supersonic Couette flow for a perfect gas governed by Sutherland viscosity law was studied using two global methods to solve the linear stability equations. The two methods are a fourth-order finite-difference method and a spectral collocation method. Two families of wave modes, modes I and II, were found to be unstable at finite Reynolds numbers, where mode II is the dominant instability among the unstable modes. These two families of wave modes are acoustic modes created by sustained acoustic reflections between a wall and a relative sonic line when the mean flow in the local region is supersonic with respect to the wave velocities. The effects of viscosity on the stability of the two families of acoustic modes were studied by comparing the viscous results at finite Reynolds numbers with the inviscid results published by Duck, Erlebacher, and Hussaini [J. Fluid Mech. **258** (1994)]. It was shown that viscosity plays a destabilizing role in both mode I and mode II stability for supersonic Couette flow in a range of Reynolds numbers and wavenumbers. The effects of compressibility, three-dimensionality, and wall cooling on the two wave families were also studied. The stability of supersonic Couette flow was found to be different from that of the unbounded boundary layers in many aspects because of the effects of additional boundary conditions at the upper wall. © *1998 American Institute of Physics.* [S1070-6631(98)01203-3]

I. INTRODUCTION

The prediction of stability and transition of hypersonic flows is critical to the accurate calculations of aerodynamic forces and heating rates for hypersonic vehicles. Much of the current understanding of the stability properties of hypersonic boundary layers comes from the linear stability theory (LST).[1–5] Mack[2,6,4,7] did extensive studies on the linear stability of compressible boundary layers and shear flows. He found that there is a new family of multiple higher instability wave modes in supersonic boundary layers. The higher modes exist when the relative flow Mach numbers at the wall are supersonic while those in the free stream are subsonic. The relative, or convective, Mach number is defined as a flow Mach number in a reference frame moving at the velocity of an instability wave. These higher modes are acoustic waves created by a substained reflection of acoustic waves in a relative supersonic region between the wall and the relative sonic line.[8] The first of the higher modes, which was labeled as the second mode by Mack, has been found to be the dominant unstable mode for a zero-pressure-gradient boundary layer over a flat plate at high Mach numbers.

Acoustic instability wave modes similar to the higher modes in compressible boundary layers have also been found in supersonic jets and mixing layers.[8–12] The effects of walls on acoustic instability modes in bounded compressible shear layers were studied in Refs. 8, 12–15. Tam and Hu[13] showed that, in contrast with the unbounded flow of supersonic boundary layers, there are two families of unstable acoustic modes when the relative Mach numbers of the flow at the walls on both sides of the shear layers are supersonic. The results indicated that the existence of the walls has a strong effect on the acoustic instability waves in the bounded compressible shear layers. These results are in agreement with Mack's conclusion on the existence of acoustic modes.[8] Therefore, for hypersonic bounded flows, such as plane Couette flow, it is expected that the stability properties will be different from those of the unbounded compressible boundary layers because of the combined effects of the upper and lower walls.

This paper is concerned with the linear stability of viscous compressible Couette flow at finite Reynolds numbers. The stability of plane Couette flow is a standard problem in fluid mechanics. Extensive studies have been done with regard to incompressible Couette flow because the exact solutions to the Navier-Stokes equations for the basic flow are available. A summary of the stability properties of incompressible Couette flow can be found in Drazin and Reid.[16] Theoretical analysis[17] and numerical solutions[18–22] have shown that the flow is always stable to infinitesimal disturbances. The first general proof of stability was given by Romanov[23] that the normal modes of the linear problem are stable for all wavenumbers $\alpha \geqslant 0$ and all Reynolds numbers $Re > 0$. However, instabilities were observed in experiments.[24,25] A number of investigations have been made to resolve the dichotomy. The evidence seems to point to the finite-amplitude effects.

The compressible stability of Couette flow, on the other hand, is much less well understood. Glatzel[26,27] studied the inviscid and viscous stability properties and normal mode structures of plane compressible Couette flow using a sim-

plified flow model of constant viscosity coefficients and a constant density profile for the basic-flow solutions. Such a model leads to a constant temperature distribution and a linear velocity profile for the basic flow. Girard[28] considered the same problem allowing for variations in density and temperature, but with a constant viscosity assumption. For practical compressible Couette flow, however, the mean temperature and density are not constant. The viscosity and heat-conductivity coefficients are functions of local temperature.

Duck *et al.*[29] studied the linear inviscid and viscous stability of compressible Couette flow using realistic compressible flow models. The viscosity coefficients were computed by the Sutherland's law with a constant Prandtl number of 0.72. Though closed-form solutions for the mean flow are not available for such viscosity law, it is straight forward to generate highly accurate numerical solutions of compressible Couette flow with little computational cost. Using numerically generated solutions for the basic flow, Duck *et al.* calculated the inviscid stability modes of compressible Couette flow. The inviscid stability characteristics of the bounded Couette flow was found to be quite different from that of the unbounded boundary layers. For supersonic Couette flow, they found two families of inviscid wave modes. For the viscous instability of compressible Couette flow, Duck *et al.* analyzed the effects of viscosity on the stability by asymptotic analysis. Viscosity was found to play a stabilizing role for the unstable modes. Duck *et al.* also obtained the spectra of viscous eigen modes numerically from the linearized full Navier-Stokes equations for the viscous stability at finite Reynolds numbers. Although the viscous unstable modes were expected to exist at high Reynolds numbers, no evidence of unstable modes was found in their numerical solutions. One of the possible reasons is the inadequate numerical resolutions in their computations for the cases of Mach 2 at high Reynolds numbers and for the cases of Mach 5. Currently, the characteristics of the instability for viscous compressible Couette flow with realistic flow model are still not clear.

The purpose of this paper is to investigate the viscous stability of compressible Couette flow at finite Reynolds numbers. To ensure numerical accuracy of the solutions, two global stability computer codes for general parallel shear flows were developed using a fourth-order finite-difference method and a Chebyshev spectral collocation method.[30] The accuracy of these two linear stability codes was first validated by comparing their stability solutions with the published solutions by Malik[30] for compressible boundary layers. The accuracy of stability solutions for compressible Couette flow was also checked by grid refinement and by comparing the solutions obtained by our two different methods. The linear stability results for compressible Couette flow were further checked by comparing with direct numerical simulations by Zhong.[31] Good agreement was observed in these comparisons. Our viscous stability results also compared well with those obtained by Duck *et al.*[29] for the case of Mach 2 Couette flow. After the validation of numerical accuracy, the viscous stability of compressible Couette flow was computed for a range of Mach numbers, wavenumbers, and Reynolds numbers. Unstable eigenmodes I and II, which correspond to the two families of inviscid acoustic modes studied by Duck *et al.*, were obtained for supersonic viscous Couette flow at finite Reynolds numbers. The characteristics of the viscous modes were investigated in details and the effects of compressibility, three-dimensionality, and wall cooling were studied. In addition, the effects of viscosity on the stability of compressible Couette flow were examined by comparing the viscous results with the inviscid stability results obtained by Duck *et al.*[29]

II. FORMULATION

A. Equations

The linear stability is considered for compressible viscous plane Couette flow confined between two infinite parallel walls located at $y^*=0$ (lower wall) and $y^*=L^*$ (upper wall), where the superscript ''*'' represents dimensional quantities. In the Cartesian coordinates, the x^*, y^*, z^* coordinates are those in the stream wise, wall-normal, and spanwise directions, respectively. The gas is assumed to be a perfect Newtonian gas. The upper wall is held at a constant temperature T_∞^* and a constant velocity U_∞^* in the x^* direction, where the flow variables at the upper wall are denoted by a subscript ''∞.'' The lower wall is stationary with either adiabatic or isothermal conditions with a wall temperature T_w^*. The three-dimensional Navier-Stokes equations are:

$$\rho^*\left[\frac{\partial \mathbf{u}^*}{\partial t^*}+\mathbf{u}^*\cdot\nabla\mathbf{u}^*\right]=-\nabla p^*+\nabla\cdot[\lambda^*(\nabla\cdot\mathbf{u}^*)\mathbf{I}+\mu^*(\nabla\mathbf{u}^*+\nabla\mathbf{u}^{*tr})], \tag{1}$$

$$\frac{\partial \rho^*}{\partial t^*}+\nabla\cdot(\rho^*\mathbf{u}^*)=0, \tag{2}$$

$$\rho^* c_p^*\left[\frac{\partial T^*}{\partial t^*}+\mathbf{u}^*\cdot\nabla T^*\right]=\nabla\cdot(k^*\nabla T^*)+\frac{\partial p^*}{\partial t^*}+\mathbf{u}^*\cdot\nabla\mathbf{u}^*+\Phi^*, \tag{3}$$

$$p^*=\rho^* R^* T^*, \tag{4}$$

where $\mathbf{u}^*$ is the velocity vector, ρ^* is the density, p^* is the pressure, T^* is the temperature, R^* is the gas constant, c_p^* is the specific heat at constant pressure, k^* is the thermal conductivity, μ^* is the first coefficient of viscosity, and λ^* is the second coefficient of viscosity. The viscous dissipation function, Φ^*, is given as

$$\Phi^*=\lambda^*(\nabla\cdot\mathbf{u}^*)^2+\frac{\mu^*}{2}[\nabla\mathbf{u}^*+\nabla\mathbf{u}^{*tr}]^2. \tag{5}$$

The flow variables and equations are nondimensionalized as follows: velocities by U_∞^*, length scales by L^*, density by ρ_∞^*, temperature by T_∞^*, pressure by $\rho_\infty^* U_\infty^{*2}$, and time scale by L^*/U_∞^*. All other variables are nondimensionalized by their corresponding values on the upper wall. The dimensionless variables are represented by the same symbols as those used for the dimensional variables but without the superscript ''*.'' The Reynolds number is defined as

$$Re=\frac{U_\infty^* \rho_\infty^* L^*}{\mu_\infty^*}, \tag{6}$$

and the Mach number is

$$M_\infty=\frac{U_\infty^*}{(\gamma R^* T_\infty^*)^{1/2}}, \tag{7}$$

where $R^*=c_p^*-c_v^*$, c_v^* is the specific heat at constant volume, and γ is the ratio of specific heats. The Prandtl number is defined as $Pr=\mu^* c_p^*/k^*$. The viscosity coefficient is determined by Sutherland's law,

$$\mu=T^{1.5}\left(\frac{1+C}{T+C}\right), \tag{8}$$

where C is a constant. In this paper, it is assumed that $C=0.5$, $\lambda=-2/3\mu$, $\gamma=1.4$, and $Pr=0.72$.

B. Basic-flow solutions

For compressible Couette flow, the steady basic-flow solutions are functions of y only, i.e., $\overline{U}=\overline{U}(y)$ and $\overline{T}=\overline{T}(y)$. Although there is no closed-form solutions for a general viscosity model, the basic-flow solution for $\overline{U}$ can be accurately and efficiently integrated by a numerical method.[32] The constant shear of Couette flow allows the temperature solution to be obtained by a quadratic algebraic relation with velocity. For the case of adiabatic lower wall, the recovery temperature at the wall is

$$T_r=1+\tfrac{1}{2}(\gamma-1)PrM_\infty^2. \tag{9}$$

Figure 1 shows the numerically obtained basic-flow velocity and temperature distributions for Couette flow at three supersonic Mach numbers with adiabatic lower wall conditions.

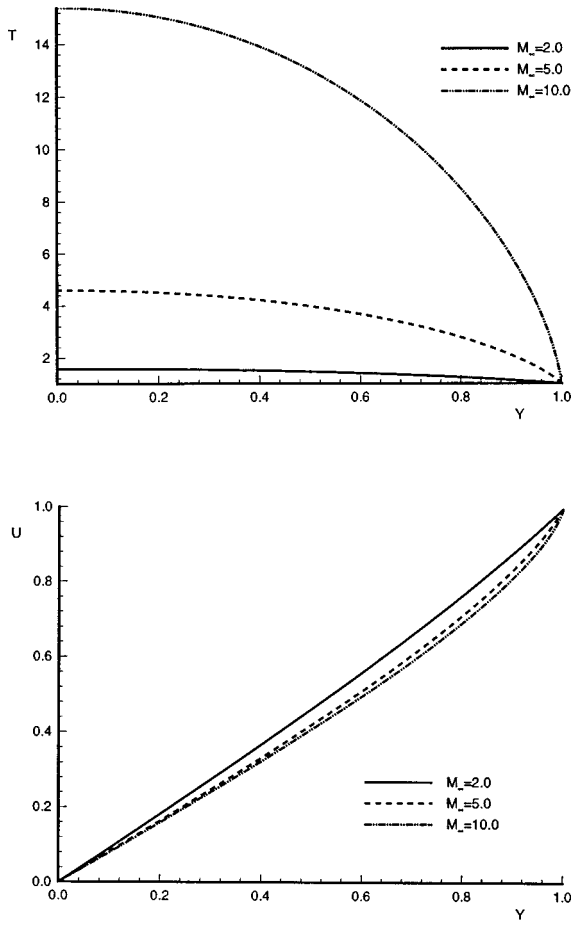

FIG. 1. Basic-flow temperature ($\overline{T}$) and velocity ($\overline{U}$) profiles at Mach 2, 5, and 10 with adiabatic lower wall.

C. Linear stability equations

The linear stability analysis is based on a normal mode analysis of the linearized perturbation equations of the three-dimensional Navier-Stokes equations. The LST formulas presented in this paper for Couette flow can be easily extended to the normal mode analysis for general compressible flows with parallel steady flow fields. The perturbation equations are derived by representing the instantaneous flow variables as a sum of a basic-flow solution and a small fluctuation quantity, i.e.,

$$\begin{aligned} u&=\overline{U}(y)+u'(x,y,z,t),\\ v&=v'(x,y,z,t),\\ w&=w'(x,y,z,t),\\ p&=\overline{p}+p'(x,y,z,t),\\ T&=\overline{T}(y)+T'(x,y,z,t). \end{aligned} \tag{10}$$

Substituting Eq. (10) into the nondimensional form of the governing Eqs. (1)–(5), and dropping the nonlinear and high-order terms yield a set of linear differential equations for the perturbation variables. Details of the linear perturbation equations and other formulations can be found in Malik.[30] The perturbation velocity and temperature satisfy homogeneous boundary conditions at the upper and lower walls. In the normal mode analysis for the linear disturbances, the fluctuations of flow quantities are assumed to be represented by harmonic waves of the following form:

$$[u',v',p',T',w']^{tr}=[\hat{u}(y),\hat{v}(y),\hat{p}(y),\hat{T}(y),\hat{w}(y)]^{tr}\times e^{i(\alpha x+\beta z-\omega t)}, \tag{11}$$

where α and β are the wavenumbers in x and z directions, respectively, and ω is the frequency of the disturbance waves. These parameters are in general complex numbers. The complex amplitude (eigen) function of a typical flow variable, say u, is $\hat{u}(y)$. Substituting Eq. (11) into the linearized perturbation equations leads to a homogeneous system of ordinary differential equations:

$$(\mathbf{A}D^2+\mathbf{B}D+\mathbf{C})\Phi=0, \tag{12}$$

where D is the derivative operator in y direction, i.e., $D=d/dy$ and $D^2=d^2/dy^2$. In the equation above, Φ is a vector defined as

$$\Phi=\begin{bmatrix}\hat{u}(y)\\ \hat{v}(y)\\ \hat{p}(y)\\ \hat{T}(y)\\ \hat{w}(y)\end{bmatrix}, \tag{13}$$

and **A**, **B** and **C**, which are 5×5 matrices, are functions of α, β, ω, Re, M_∞, and the basic-flow solutions. The detailed expressions of matrices **A**, **B** and **C** can be found in Ref. 30, and they are not repeated here. The boundary conditions for Eq. (12) are no-slip conditions for velocities at both walls, isothermal temperature condition at the upper wall, and adiabatic condition for the lower wall, i.e.,

$$\hat{u}(1)=\hat{v}(1)=\hat{w}(1)=\hat{u}(0)=\hat{v}(0)=\hat{w}(0),$$

$$\hat{T}(1)=\frac{\partial\hat{T}}{\partial y}(0)=0. \tag{14}$$

In the case of isothermal condition for the lower wall, the temperature condition at $y=0$ is replaced by $\hat{T}(0)=0$. The above temperature perturbation boundary conditions are used to be in accordance with Duck *et al.*[29] In fact, $\hat{T}(0)=0$ is a more physical condition to use regardless of the basic flow boundary conditions. Nonetheless, it is found that this boundary condition does not affect the main stability characteristics of the flow.

The homogeneous equation system (12) and homogeneous boundary conditions (14) form an eigenvalue problem. For plane compressible Couette flow, the temporal linear stability is considered, i.e., for a given set of real-value α and β, ω is solved as an eigenvalue of the homogeneous boundary value problem given by Eqs. (12) and (14):

$$\omega=\omega(\alpha,\beta,Re,M_\infty). \tag{15}$$

Meanwhile, The amplitude of the disturbance modes, $[\hat{u}(y),\hat{v}(y),\hat{p}(y),\hat{T}(y),\hat{w}(y)]^{tr}$, is solved as an eigenfunction of the boundary value problem. The real part of ω, $\mathrm{Re}\{\omega\}$, represents the frequency of the disturbance modes, while the imaginary part, $\mathrm{Im}\{\omega\}$, represents the temporal amplification rate of the disturbances. When $\mathrm{Im}\{\omega\}$ is greater, equal to, or smaller than 0, a disturbance mode is unstable with finite amplification, neutrally stable, or stable with finite damping, respectively. We also define a complex wave (phase) velocity c of the disturbance waves as $c=\omega/\alpha$. The disturbance waves are three dimensional in general. Two-dimensional disturbance modes correspond to a special case of $\beta=0$.

III. NUMERICAL METHODS AND VALIDATION

For a given set of real-value α and β, the temporal stability analysis solves ω and Φ as eigenvalues and eigenfunctions of the homogeneous boundary value problem given by Eqs. (12) and (14). Various numerical methods for solving the eigenvalue problem of the linear stability equations for hypersonic boundary layers were discussed and evaluated by Malik.[30] The eigenvalue problem can be solved by either global or local methods. A global method computes all the eigenvalues of the discretized system, while a local method only solves for a single eigenvalue and its eigenfunctions. The global methods are usually computationally more expensive, but they have the advantage of obtaining the whole set of eigenvalues and eigenfunctions at the same time. On the other hand, the local methods are limited to solving a single set of eigenvalue and eigenfunction only, but they are usually more computationally efficient than global methods. In this paper, the eigen spectra of the eigenvalue problem are computed by global methods using two different discretization methods. The first method is a fourth-order finite-difference method (4FD), and the second method is a Chebyshev spectral collocation method (SC) described by Malik.[30] The comparisons of the results from the two different discretization methods are useful in determining the numerical resolution of the results and in separating spurious numerical eigen modes from the physical ones in the solutions.

A. Fourth-order finite-difference global (4FD) method

In the finite-difference method, Eq. (12) is discretized by fourth-order finite-difference approximations to D and D^2 derivative operators. In implementing the fourth-order finite-difference method, we use a non-staggered grid. One-sided difference formulas are used to approximate the first-order derivatives of $\hat{p}$ on the walls. The following formulas are derived based on uniformly distributed grid points, whose index j is from 1 to $N+1$. The lower wall ($y=0$) corresponds to $j=1$, while the upper wall ($y=1$) corresponds to $j=N+1$. The fourth-order finite-difference formulas at a grid point j are listed below.

For $3\leqslant j\leqslant N-1$:

$$D^2\Phi_j=\frac{1}{12\Delta y^2}(-\Phi_{j+2}+16\Phi_{j+1}-30\Phi_j+16\Phi_{j-1}-\Phi_{j-2}), \tag{16}$$

$$D\Phi_j=\frac{1}{12\Delta y}(-\Phi_{j+2}+8\Phi_{j+1}-8\Phi_{j-1}+\Phi_{j-2}). \tag{17}$$

For $j=2$:

$$D^2\Phi_j=\frac{1}{12\Delta y^2}(10\Phi_{j-1}-15\Phi_j-4\Phi_{j+1}+14\Phi_{j+2}-6\Phi_{j+3}+\Phi_{j+4}), \tag{18}$$

$$D\Phi_j=\frac{1}{12\Delta y}(-3\Phi_{j-1}-10\Phi_j+18\Phi_{j+1}-6\Phi_{j+2}+\Phi_{j+3}). \tag{19}$$

For $j=N$:

$$D^2\Phi_j=\frac{1}{12\Delta y^2}(\Phi_{j-4}-6\Phi_{j-3}+14\Phi_{j-2}-4\Phi_{j-1}-15\Phi_j+10\Phi_{j+1}), \tag{20}$$

$$D\Phi_j=\frac{1}{12\Delta y}(-\Phi_{j-3}+6\Phi_{j-1}-18\Phi_{j-1}+10\Phi_j+3\Phi_{j+1}). \quad (21)$$

The first derivatives of $\hat{p}$ near the wall are given below. For $j=2$:

$$D\Phi_j=\frac{1}{12\Delta y}(-25\Phi_j+48\Phi_{j+1}-36\Phi_{j+2}+16\Phi_{j+3}-3\Phi_{j+4}). \quad (22)$$

For $j=3$:

$$D\Phi_j=\frac{1}{12\Delta y}(-3\Phi_{j-1}-10\Phi_j+18\Phi_{j+1}-6\Phi_{j+2}+\Phi_{j+3}). \quad (23)$$

For $j=N$:

$$D\Phi_j=\frac{1}{12\Delta y}(3\Phi_{j-4}-16\Phi_{j-3}+36\Phi_{j-2}-48\Phi_{j-1}+25\Phi_j). \quad (24)$$

For $j=N-1$:

$$D\Phi_j=\frac{1}{12\Delta y}(-\Phi_{j-3}+6\Phi_{j-2}-18\Phi_{j-1}+10\Phi_j+3\Phi_{j+1}). \quad (25)$$

In the above equations, a uniform grid size Δy is assumed.

Discretized Eq. (12) using the fourth-order finite-difference formulas given above, along with the homogeneous boundary conditions at the walls given by Eq. (14), leads to a matrix eigenvalue problem:

$$\mathbf{A}'\mathbf{\Phi}=\omega\mathbf{B}'\mathbf{\Phi}, \quad (26)$$

where ω is the eigenvalue, $\mathbf{A}'$ and $\mathbf{B}'$ are $5(N-1)\times 5(N-1)$ matrices for the case of isothermal lower wall and $(5N-4)\times(5N-4)$ matrices for the case of adiabatic lower wall, and $\mathbf{\Phi}$ is the discrete representation of the eigenfunction at the grid points, i.e.,

$$\mathbf{\Phi}=[\Phi_2,\ldots,\Phi_N]^{tr} \quad \text{(Isothermal)}, \quad (27)$$

$$\mathbf{\Phi}=[\Phi_1,\ldots,\Phi_N]^{tr} \quad \text{(Adiabatic)}. \quad (28)$$

The whole eigenvalue spectrum and eigenfunctions can be obtained numerically by solving Eq. (26) using the QZ eigenvalue algorithm of the IMSL computer subroutine library.

In the actual calculations, a stretched grid is used to distribute more grid points near the walls. A coordinate transformation is used to transform the equation in the non-uniform coordinates into uniform computational ones. A natural choice for the stretching function in the coordinate transformation for solving Couette flow is

$$y=\frac{1-\cos\pi\eta}{2}, \quad (29)$$

where $\eta\in[0,1]$ is the computational coordinate and $y\in[0,1]$ is the physical coordinate. However, this transformation has a singularity in $\partial\eta/\partial y$ at the walls. Therefore, a modified transformation is used,

$$y=\frac{\cos\pi\eta-\cos\pi\Delta}{\cos[\pi(1-\Delta)]-\cos\pi\Delta}, \quad (30)$$

where Δ is chosen to be 0.001, $\eta\in[\Delta,1-\Delta]$, and $y\in[0,1]$.

B. Chebyshev spectral collocation global (SC) method

The solution procedure for the spectral collocation global method is the same as that for the finite-difference method except that a Chebyshev polynomial is used in the discretization of Eq. (12). The Chebyshev spectral collocation discretization method used in this paper follows that given by Malik[30] for his single domain spectral collocation method (SDSP). The Nth-order Chebyshev polynomials T_N are defined on the interval $\xi_j\in[-1,1]$. The collocation points ξ_j, which are the extrema of T_N, are

$$\xi_j=\cos\frac{\pi j}{N}, \quad j=0,1,\ldots,N. \quad (31)$$

In order to apply the spectral collocation method, an interpolant polynomial is constructed for the dependent variables in terms of their values at the collocation points. A Nth-order polynomial is

$$\Phi(\xi)=\sum_{k=0}^{N}\lambda_k(\xi)\Phi(\xi_k), \quad (32)$$

where the interpolant $\lambda_k(\xi)$ for the Chebyshev scheme is

$$\lambda_k(\xi)=(-1)^{(k+1)}\left(\frac{1-\xi_k^2}{\xi-\xi_k}\right)\frac{T_N'(\xi)}{N^2c_k}, \quad (33)$$

where $c_0=c_N=2$, and $c_k=1$ for $0<k<N$. From Eq. (32), the first derivative of $\Phi(\xi)$ can be written as

$$\left.\frac{d\Phi}{d\xi}\right|_j=\sum_{k=0}^{N}E_{jk}\Phi_k, \quad (34)$$

where E_{jk} are the elements of the derivative matrix defined as:

$$E_{jk}=\frac{c_j}{c_k}\frac{(-1)^{k+j}}{\xi_j-\xi_k}, \quad \text{for } j\neq k, \quad (35)$$

$$E_{jj}=-\frac{\xi_j}{2(1-\xi_j^2)}, \quad (36)$$

$$E_{00}=-E_{NN}=\frac{2N^2+1}{6}. \quad (37)$$

The transformation between physical and computational domains is

$$\xi_j=2y_j-1, \quad \text{where } y\in[0,1]. \quad (38)$$

The scaling factor for the transformation between physical domain y and computational domain ξ is thus given as

$$S_j=\left.\frac{\partial \xi}{\partial y}\right|_j=2, \quad j=0,1,\ldots,N, \tag{39}$$

then the first derivative matrix F in the physical domain may be written as

$$F_{jk}=S_j E_{jk}, \tag{40}$$

and the second derivative matrix G_{jk} is

$$G_{jk}=F_{jm}F_{mk}. \tag{41}$$

Now the governing equation (12) can be written at the collocation points as

$$A_j\sum_{k=0}^{N} G_{jk}\Phi_k+B_j\sum_{k=0}^{N} F_{jk}\Phi_k+C_j\Phi_j=0. \tag{42}$$

The Neumann boundary condition for temperature eigenfunction at the lower wall is enforced using:

$$\left.\frac{d\hat{T}}{dy}\right|_{y=0}=\sum_{k=0}^{N} F_{Nk}T_k=0. \tag{43}$$

The Neumann conditions for pressure eigenfunction are enforced as

$$\left.\frac{\partial \hat{p}}{\partial y}\right|_{y=0}=a, \quad \left.\frac{\partial \hat{p}}{\partial y}\right|_{y=1}=b, \tag{44}$$

where a and b are evaluated at the two boundaries using the normal momentum equations. The approximation by Eq. (42) and the boundary conditions lead to a matrix eigenvalue problem which has the same form as that of Eq. (26) except that $\mathbf{\Phi}$ contains $5N-2$ elements instead of $5N-4$ elements as in the fourth-order finite-difference scheme. Again, the eigenvalue problem is solved numerically by the QR matrix eigenvalue subroutine of the IMSL library.

C. Results validation and numerical accuracy

The two linear stability codes using the fourth-order finite-difference method and the spectral collocation method were first validated by comparing their solutions with those of Malik[30] for the linear stability of the flat-plate compressible boundary layer. The solution procedures for the linear stability of compressible boundary layer are the same as those for Couette flow except that the basic-flow profiles and the boundary conditions are different. Malik[30] tested various numerical schemes for solving the temporal boundary layer linear stability problem in five test cases. The comparison of the present results with Malik's results for these five test cases are similar. Only the comparison of the present results with Malik's results for his test case 3 is shown in Table I. The flow conditions for this test case are compressible boundary layer over a flat plate with zero pressure gradient at $M_\infty=2.5$, $Re=3000$, $T_0=600^0R$, and $T_w/T_{adb}=1$. In the table, the results of three methods used by Malik are compared with our results. The three methods used by Malik are a fourth-order compact finite-difference (4CD) scheme, a single domain spectral collocation (SDSP) method, and a multi-domain spectral collocation (MDSP) method. In our calculations, an exponential grid stretching function was used for the boundary layer in the fourth-order finite-difference global (4FD) method, while the stretching function for our spectral collocation global (SC) method followed the stretching function described in Malik[30] for his SDSP scheme. For each scheme, Malik[30] first used a global method to compute all the eigenvalues of the discretized system, and then used a local method to purify the eigenvalues obtained by the global method and the associated eigenfunctions. Better accuracy may be achieved when both the global and local methods are used than that obtained by the global method only using the same grid points. Since our numerical methods are only global ones, more grid points were used in comparing our results with those from Malik. Table I shows that our numerical results agree very well with Malik's results.

TABLE I. The eigenvalue solutions of complex frequency ω for the temporal linear stability of a compressible boundary layer ($M_\infty=2.5$, $Re=3000$, $T_0=600^0R$, $T_w/T_{adb}=1$, $\alpha=0.06$, and $\beta=0.1$).

Methods	Grids	Re{ω}	Im{ω}
4CD (Malik)	61	0.0367321	0.0005847
SDSP (Malik)	61	0.0367339	0.0005840
MDSP (Malik)	61	0.0367340	0.0005840
SC (Hu and Zhong)	100	0.0367337	0.0005845
4FD (Hu and Zhong)	100	0.0367338	0.0005840

For the linear stability computations of compressible Couette flow, the solutions of present methods were validated first by comparing with the viscous solutions of Duck *et al.*[29] for a case of relatively low Mach number and low Reynolds number and then by comparing with the direct numerical simulation results by Zhong.[31] The numerical accuracy of the stability results was also evaluated by grid refinement studies and by comparing the solutions from our two methods.

Figure 2 compares the phase velocity spectra for compressible Couette flow at $M_\infty=2$, $Re=2\times10^5$, and $\alpha=0.1$ computed using our 4FD and SC methods. These results are compared with those by Duck *et al.*[29] Duck *et al.* did not solve the z-momentum equation for their two-dimensional linear stability computations. Therefore their two-dimensional spectrum contains less modes because the z-direction modes are not present in their results. The figure shows that the eigenvalue spectrum of Duck *et al.* agrees well with those from the 4FD and SC methods except that z-direction modes are not present in their two-dimensional results. In addition, the eigenvalues and eigenfunctions for compressible Couette flow obtained by our linear stability codes were also compared with the DNS simulation conducted by Zhong.[31] Excellent agreement was obtained and details can be found in Ref. 31.

The quantitative numerical accuracy of our solutions for the linear stability of compressible Couette flow was evaluated by a grid refinement study. Table II shows the grid refinement results for the two test cases using the SC method. The numerical accuracy of resolving the most im-

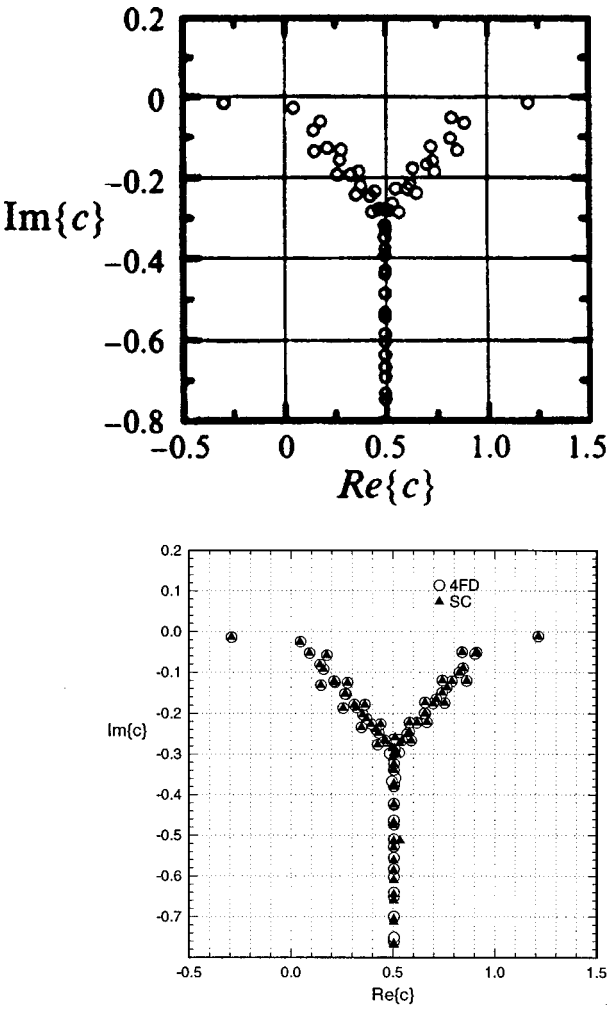

FIG. 2. Phase velocity spectrum of compressible Couette flow at $M_\infty=2$, $Re=2\times10^5$, and $\alpha=0.1$ using 100 grid points. Results of the 4FD and SC methods in the lower figure are compared with those of Duck *et al.* (1994) in the upper figure.

portant modes, modes I and II, are shown for three sets of grids. The SC method resolves modes I and II with an accuracy in the order of 10^{-10} in relative errors for case 1 of $M_\infty=2$, $Re=2\times10^5$, and $\alpha=0.1$. The accuracy is 10^{-8} or better in relative errors for case 2 at $M_\infty=5$, $Re=5\times10^6$, and $\alpha=2.1$ with grid points $N=200$.

The phase velocity spectra computed by using three sets of grids for the case of $M_\infty=5$, $Re=5\times10^6$, and $\alpha=0.1$ are shown in Fig. 3 to demonstrate the result convergence as the numbers of grid points increase. The main focus of stability analysis of the compressible Couette flow is on the least stable modes, i.e., modes I and II located near the line of Im $\{c\}=0$. The figure shows that these least stable modes are resolved very well with 100 grid points. On the other hand, 300 grid points are needed to resolve the highly damped modes with negative Im$\{c\}$ of large magnitudes. These highly damped modes are much less important to the instability of compressible Couette flow and they are not the focus of the current linear stability studies. Overall, the accuracy of the numerical solutions for modes I and II is adequate using either the 4FD and SC methods with 100 grid points. In general, the grid points needed for the same accuracy increase as Reynolds number or wavenumber increases.

In general, the condition $\hat{T}(0)=0$ should be used instead of $(d\hat{T}/dy)(0)=0$ for the temperature fluctuation at the lower wall even when the basic flow is adiabatic. The use of the temperature fluctuation boundary conditions at the wall was discussed by Malik.[30] In fact, $\hat{T}(0)=0$ is used when comparing to Malik's boundary layer linear stability results in Table I. However, we used the $(d\hat{T}/dy)(0)=0$ condition for Couette flow with an adiabatic lower wall in order to compare with the results by Duck *et al.*,[29] who used the $(d\hat{T}/dy)(0)=0$ condition for an insulated wall. Therefore, most of the results presented here are computed using $(d\hat{T}/dy)(0)=0$. Fortunately, the use of $(d\hat{T}/dy)(0)=0$ in-

TABLE II. The eigenvalue solutions of wave speed c for compressible Couette flow using the spectral collocation method with three sets of grid.

Grids	c_r	Δc_r	c_i	Δc_i
	(a) Test case 1. $M_\infty=2$, $Re=2\times10^5$, and $\alpha=0.1$			
	(Mode I)			
100	1.213965119859	0.05×10^{-10}	-0.011585118523	0.35×10^{-10}
200	1.213965119817	0.37×10^{-10}	-0.011585118448	1.10×10^{-10}
300	1.213965119854	–	-0.011585118558	–
	(Mode II)			
100	-0.291572925106	0.02×10^{-11}	-0.013821128462	0.05×10^{-11}
200	-0.291572925140	0.32×10^{-11}	-0.013821128536	0.79×10^{-11}
300	-0.291572925108	–	-0.013821128457	–
	(b) Test case 2. $M_\infty=5$, $Re=5\times10^6$, and $\alpha=2.1$			
	(Mode I)			
100	0.972869314676	0.42×10^{-7}	-0.003456356315	0.11×10^{-6}
200	0.972869272448	0.20×10^{-11}	-0.003456466520	0.20×10^{-11}
300	0.972869272450	–	-0.003456466522	–
	(Mode II)			
100	0.040730741952	0.79×10^{-5}	0.000876050503	0.95×10^{-5}
200	0.040722854287	0.13×10^{-8}	0.000885530891	0.53×10^{-9}
300	0.040722853034	–	0.000885531421	–

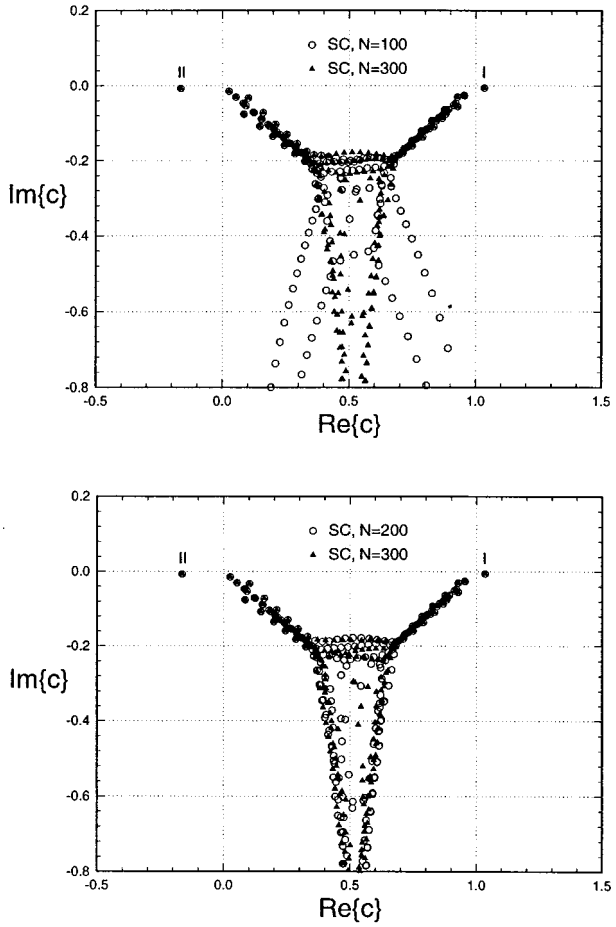

FIG. 3. Phase velocity spectra obtained using different number of grid points for compressible Couette flow at $M_\infty=5$, $Re=5\times10^6$, and $\alpha=0.1$.

stead of $\hat{T}(0)=0$ does not make a significant difference on the results presented in this paper. This is illustrated in Table III which gives the comparisons of mode I and II eigenvalues computed by using the two boundary conditions in a case of $M_\infty=5.0$, $\alpha=3.0$, and $Re=5\times10^5$ with 101 and 201 grid points. The table shows that the differences in the results obtained by using the two sets of boundary conditions are a few percent. In addition, mode II is affected less by the boundary conditions than mode I. The overall impact of using different boundary conditions is not significant. This is further shown in Fig. 4 where the eigenfunctions of the unstable mode II obtained using the two different temperature fluctuation boundary conditions at the lower wall are compared. The only noticeable difference is in temperature disturbance $\hat{T}(y)$ at the region close to the lower wall. The pressure perturbation is almost not affected by the use of different boundary conditions.

Having validated the accuracy of our numerical codes, viscous stability characteristics of compressible Couette flow was studied by numerical computations of viscous eigen modes for a range of Mach numbers and Reynolds numbers. Spurious modes were discussed by Malik[30] for the global spectral collocation method. Since both our methods are global methods, spurious modes were also observed in the results from both the 4FD and the SC methods. Fortunately spurious modes were easy to identify by comparing the results from the 4FD and SC methods because different methods usually give different spurious modes. Furthermore, the spurious modes are grid dependent. Therefore, in order to weed out potential spurious numerical modes in the solutions, the eigenvalue spectra presented in this paper are resolved using either both the SC and the 4FD methods or the SC method with two sets of grids.

IV. RESULTS

A. Origin of acoustic wave modes

Duck *et al.*[29] studied the inviscid stability of supersonic Couette flow and found that there are two families of inviscid wave modes. They labeled these two families of modes as the odd modes (modes I, III, etc.) and the even modes

TABLE III. The eigenvalue solutions of wave speed c at $M_\infty=5$, $Re=5\times10^5$, and $\alpha=3.0$ for plane Couette flow using the spectral collocation method with different temperature boundary conditions.

Mode	$\mathrm{Re}\{c\},\hat{T}'(0)=0$	$\mathrm{Re}\{c\},\hat{T}(0)=0$	$\mathrm{Im}\{c\},\hat{T}'(0)=0$	$\mathrm{Im}\{c\},\hat{T}(0)=0$
		(a) 101 Grid points		
Mode II	0.180269087	0.180275543	0.000139605	0.000144231
Difference	0.000006456		0.000004626	
Percentage(%)	0.00358		3.21	
Mode I	0.795060364	0.793790805	−0.012551839	−0.013756970
Difference	0.001269559		0.001205131	
Percentage(%)	0.160		8.76	
		(b) 201 Grid points		
Mode II	0.180269212	0.180275668	0.000139569	0.000144195
Difference	0.000006456		0.000004626	
Percentage(%)	0.00358		3.21	
Mode I	0.795060364	0.793790805	−0.012551839	−0.013756970
Difference	0.001269559		0.001205131	
Percentage(%)	0.160		8.76	

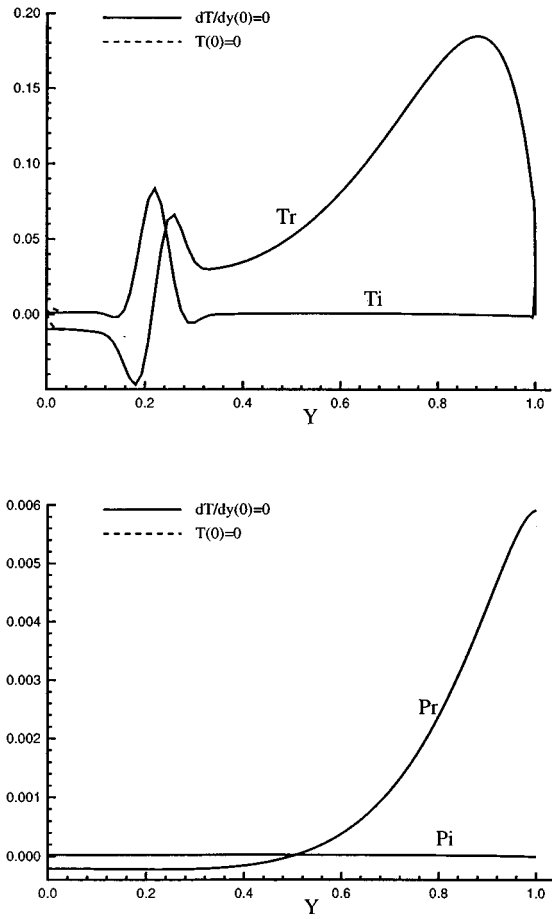

FIG. 4. Eigenfunctions of the unstable mode II using different temperature perturbation boundary conditions. $\hat{T}$ is shown in the upper figure. $\hat{p}$ is shown in the lower figure.

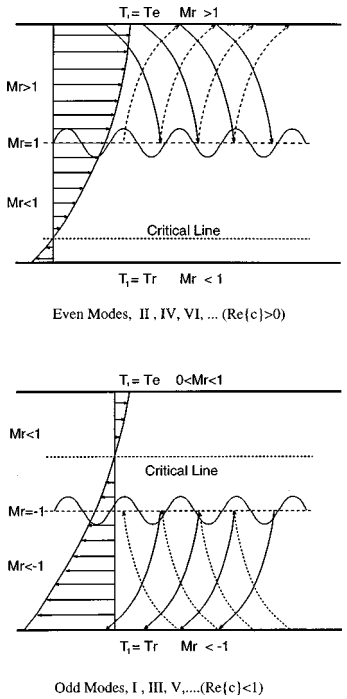

FIG. 5. A schematic of the Mach waves and the two families of acoustic wave modes in supersonic Couette flow in reference frames moving at the velocity of the disturbance waves (Re$\{c\}$ is the wave speed of an acoustic mode).

(modes II, IV, etc.). For the case of Mach 2, the odd modes are defined as the inviscid modes with Re$\{c\}$ larger than 1 and Im$\{c\}=0$ (neutrally stable) as wavenumber α approaches zero. As α increases, the wave speed Re$\{c\}$ of the odd modes decreases. On the other hand, the even modes are defined as the inviscid modes with Re$\{c\}$ less than 0 and Im $\{c\}=0$ as α approaches zero. As α increases, the wave speed Re$\{c\}$ of the even modes increases. Both families of the inviscid modes are neutrally stable when Re$\{c\}>1$ (for odd modes) or Re$\{c\}<0$ (for even modes). Duck *et al.*[29] showed that, if $0<\mathrm{Re}\{c\}<1$, the necessary condition for the existence of neutral stability modes in compressible Couette flow is that there is a generalized inflection point (GIP) in $0<y<1$. Similar to the case of compressible boundary layers,[1] the generalized inflection point is defined as

$$\frac{d}{dy}\left[\overline{U_y}/\overline{T}\right]=0. \tag{45}$$

For compressible Couette flow with an adiabatic lower wall, there is no GIP inside the flow channel. A GIP occurs only if the basic-flow temperature profile has a local extremum, which implies that the lower wall must be cooled below the adiabatic condition. For compressible Couette flow with an adiabatic lower wall, Duck *et al.* found that, when $0<\mathrm{Re}\{c\}<1$, both even and odd modes are no longer neutrally stable. Under this condition, the odd modes become stable with finite damping, but the even modes become unstable, where mode II has the largest growth rate among the unstable even modes.

The two families of inviscid modes in supersonic Couette flow are similar in origin to the acoustic instability modes for supersonic flows with one, two and no boundaries studied by Mack[4,8] and the acoustic instability wave modes of supersonic mixing layers inside a rectangular channel studied by Tam and Hu.[13] The physical mechanism of such inviscid acoustic modes can be explained by considering a wave in a moving reference frame traveling at the wave speed. The necessary condition for the existence of such acoustic modes is that there is a region of locally supersonic flow relative to the phase speed of the instability wave. Acoustic wave modes are formed by substained wave reflections between the walls and the relative sonic line. Compared with a single family of acoustic modes for the unbounded compressible boundary layers, there are two families of acoustic modes for the bounded Couette flow because there is one family of modes for each of the upper and lower walls. Figure 5 shows a schematic of the two families of acoustic modes in supersonic Couette flow in reference frames moving with the waves. Specifically, the odd wave modes are formed by substained acoustic reflections between the lower wall and the relative sonic line, and the even wave modes are formed by the acoustic reflections between the upper wall and the relative sonic line. In general, these two families of acoustic modes are not symmetric with respect to the center line $y=1/2$ because the basic-flow temperature and velocity

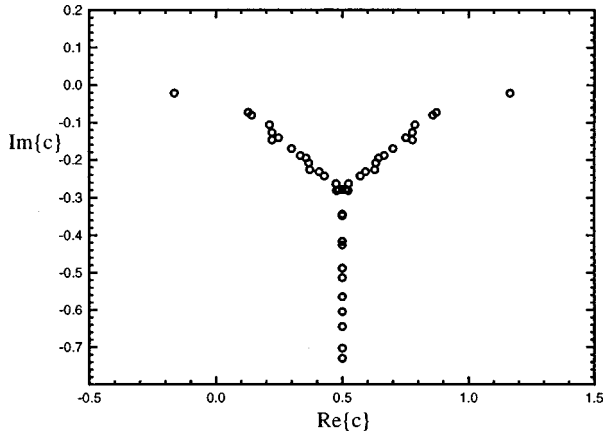

FIG. 6. Eigenvalue spectrum at $M_\infty=2.0$, $Re=5\times10^4$, and $\alpha=0.1$ with isothermal basic-flow lower wall temperature conditions.

profiles are not symmetric as shown in Fig. 1. Duck *et al.* found that, for the case of adiabatic lower wall in the inviscid limit, when $0<\mathrm{Re}\{c\}<1$, the odd modes are in general stable with finite damping and even modes are unstable. When the upper and lower wall temperatures are the same, the eigenvalue spectra become symmetric about the $\mathrm{Re}\{c\}=0.5$ line. An eigenvalue spectrum at $M_\infty=2.0$, $Re=5\times10^4$, and $\alpha=0.1$ with isothermal lower wall is shown in Fig. 6. The figure shows that the corresponding even and odd modes are symmetric with respect to the $\mathrm{Re}\{c\}=0.5$ line.

B. Eigenmode spectra

Using the new global methods, we have obtained unstable modes for supersonic viscous Couette flow at finite Reynolds numbers. Among the unstable viscous modes, mode II was found to be the dominant instability for compressible Couette flow. On the other hand, mode I, which was found to be stable in the inviscid solutions by Duck *et al.*, was also found to be unstable at finite Reynolds numbers which indicates that viscosity plays a destabilizing role. Mode I is only slightly unstable for a small range of wavenumbers when Mach number is around 3, but mode II is unstable for a large range of wavenumbers and Mach numbers. Although very weak higher mode instabilities were found in the inviscid solutions in Ref. 29, they were not found in the present viscous computations because of the magnitudes of Reynolds numbers used in the viscous computations were limited by the resolution of the numerical solutions.

Figure 7 shows the phase velocity eigenvalue spectrum for the case of $Re=5\times10^5$ and Mach 5 at a small wavenumber $\alpha=0.1$. The results shown in this paper are for the case of adiabatic lower wall except indicated otherwise. The results of the two methods are plotted in the same figure in order to identify the spurious modes in the numerical solutions. Similar to the Mach 2 case, the eigenvalue spectrum of Mach 5 flow consists a ''Y'' shaped structure located at a region of $\mathrm{Re}\{c\}$ between 0 and 1, and two families of inviscid acoustic modes located at $\mathrm{Re}\{c\}<0$ for the even modes or $\mathrm{Re}\{c\}>1$ for the odd modes. The wave modes of the

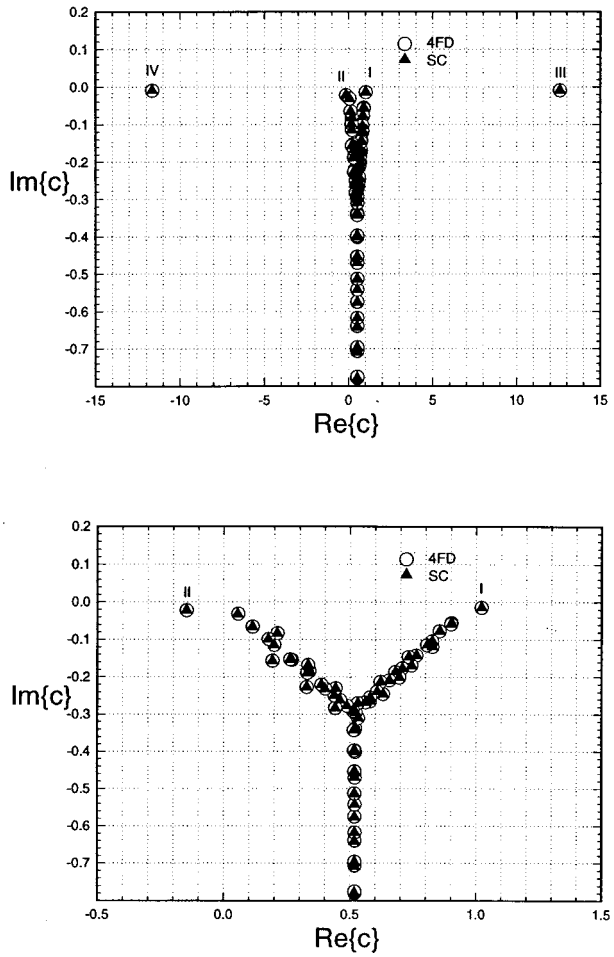

FIG. 7. Phase velocity spectrum for compressible Couette flow at $M_\infty=5$, $Re=5\times10^5$, and $\alpha=0.1$ (upper figure). A localized region of the spectrum is shown in the lower figure. The results obtained by both the 4FD and the SC methods are shown for comparison.

''Y'' shaped structure are the wave modes corresponding to the compressible extension of viscous modes in the incompressible flow. On the other hand, the acoustic modes are the results of acoustic wave reflections in the supersonic relative flow. The mode numbers of the acoustic modes, which are also located close to the line of $\mathrm{Im}\{c\}=0$, are marked in the figure. For $\alpha=0.1$, the wave velocities of the even modes (modes II, IV, ...) satisfy $\mathrm{Re}\{c\}<0$, while those of odd modes (modes I, III, ...) satisfy $\mathrm{Re}\{c\}>1$. The inviscid limit of these modes are neutral modes with $\mathrm{Im}\{c\}=0$ as shown by Ref. 29. Figure 7 shows that all these acoustic modes for viscous flow are stable due to the effects of viscosity. The figure also shows that the modes are not symmetric with respect to the line of $\mathrm{Re}\{c\}=0.5$ because the basic-flow velocity and temperature are not symmetric about the center line.

Figures 8 to 10 show the eigenvalue spectra of Couette flow with the same Mach number 5 and Reynolds number $Re=5\times10^5$ at larger wavenumbers of $\alpha=2.5$, 3.5, and 4.8, respectively. Consistent with the inviscid theory,[29] the figures show that, when wavenumber increases, $\mathrm{Re}\{c\}$ of the even modes increases while that of the odd modes decreases. Figure 8 shows that at $\alpha=2.5$, mode II becomes

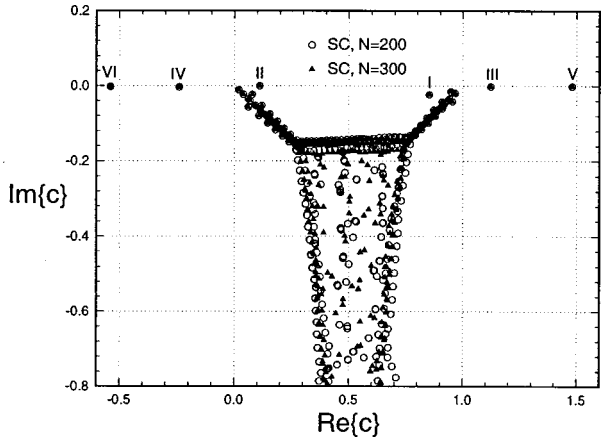

FIG. 8. Phase velocity spectrum for compressible Couette flow at $M_\infty=5$, $Re=5\times10^5$, and $\alpha=2.5$. The results obtained by the SC method using two sets of grids are shown for comparison.

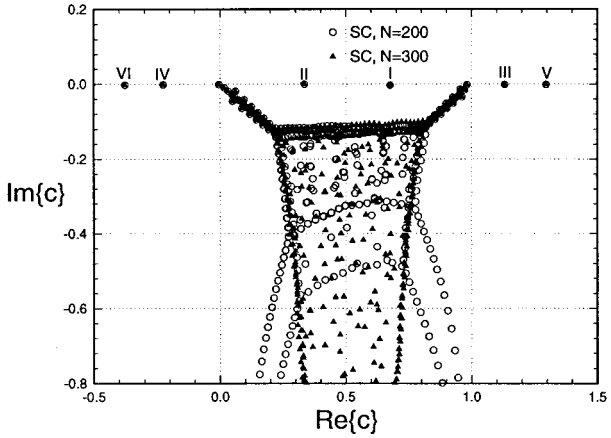

FIG. 10. Phase velocity spectrum for compressible Couette flow at $M_\infty=5$, $Re=5\times10^5$, and $\alpha=4.8$.

unstable with $\mathrm{Re}\{c\}>0$, while mode I is stable with finite damping and $\mathrm{Re}\{c\}<1$. In addition, as α increases, the original ''Y'' structure graduately evolves into a ''H'' like structure with two separated (near vertical) branches connected by three (near horizontal) bands near the original triple point. These two near vertical branches separated further as α increases in Figs. 9 and 10. The eigenvalue spectrum at a high Reynolds number is shown in Fig. 3, which plots the eigenvalue spectrum at Mach 5, $\alpha=0.1$, and $Re=5\times10^6$. The figure shows that as Reynolds numbers increase, the ''Y'' structure is again split into a two separated branches on both sides of the $\mathrm{Re}\{c\}=0.5$ line similar to the case of higher wavenumber α at $Re=5\times10^5$. The inviscid acoustic modes are closer to the neutral stability line because of this higher Reynolds number.

In addition to converged physical modes, Figs. 8 to 10 and Fig. 3 also show scattered modes with $\mathrm{Im}\{c\}$ around -0.2 or less. These scattered modes are spurious numerical modes, which will disappear if sufficiently more grid points are used in the computations. They can be easily identified in the figures because they change with different sets of grid points. As Reynolds number or wavenumber increases, more grid points are needed in the computations in order to resolve the eigenvalues in the neighborhood of the triple point of the ''Y'' or ''H'' shaped structures. This phenomenon agrees with the conclusion by Reddy *et al.*[33] that this region of spectra is sensitive to very small errors in the linear matrix elements. As a consequence, 300 grid points were used in the computations in order to resolve the eigenvalues in that region. On the other hand, the numerical accuracy of the acoustic modes, which are above the triple point region, is sufficiently accurate using 100 or 200 grid points.

The eigenfunctions of the acoustic modes shown in Fig. 8 are examined by plotting the contours of the pressure disturbances of the acoustic modes given by

$$\mathrm{Re}\{p'\}=\mathrm{Re}\{\hat{p}(y)e^{(\alpha x-\omega t)}\}. \tag{46}$$

Figure 11 shows the contours of pressure disturbances of modes II and IV over one spatial period at $M_\infty=5$, $Re=5\times10^5$, and $\alpha=2.5$ at a given time. The relative sonic line defined as

$$\hat{M}=\frac{(u-c_r)}{\sqrt{T}}M_\infty=\pm1 \tag{47}$$

is plotted with the mode II wave pattern in the figure. The eigenfunction contours of these even modes show the characteristics of standing wave pattern between upper wall and the relative sonic line as described by the schematic shown in Fig. 5. These acoustic modes are created by acoustic reflections between the upper wall and the relative sonic line. The standing wave patterns are less obvious for higher modes because the supersonic region covers most of the range between the two walls. On the other hand, Fig. 12 shows the eigenfunction contours of modes I and III. This figure shows the characteristics of standing wave patterns between the lower wall and the relative sonic line. The wave patterns and the positions of the relative sonic lines do confirm the theory that the odd modes are acoustic waves reflecting between the relative sonic line and the lower wall, while the even modes are those reflecting between the relative sonic line and the upper wall.

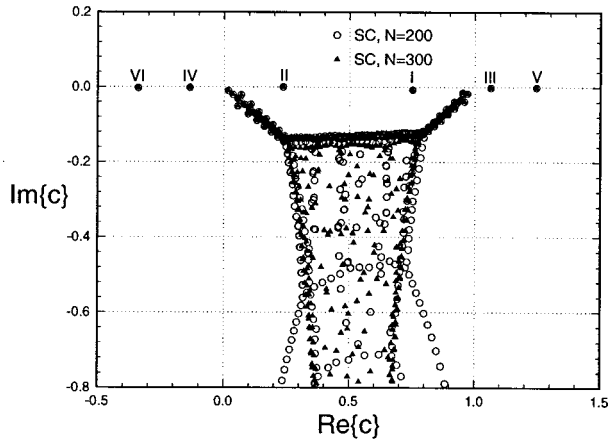

FIG. 9. Phase velocity spectrum for compressible Couette flow at $M_\infty=5$, $Re=5\times10^5$, and $\alpha=3.5$.

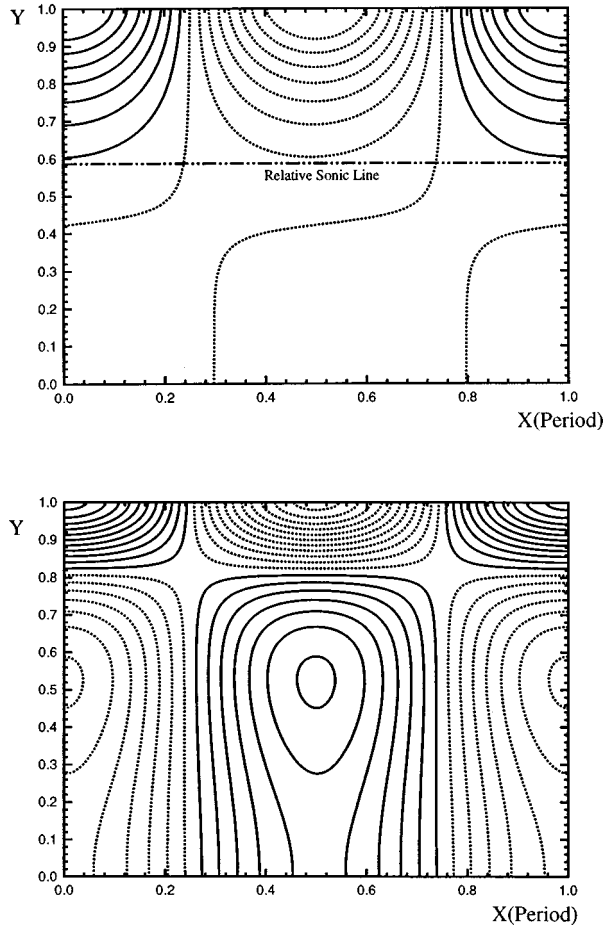

FIG. 11. The contours of the pressure perturbation for the even acoustic modes (upper figure, mode II; lower figure, mode IV) at $M_\infty=5$, $Re=5\times10^5$, and $\alpha=2.5$. Solid and dashed lines represent positive and negative perturbation levels, respectively.

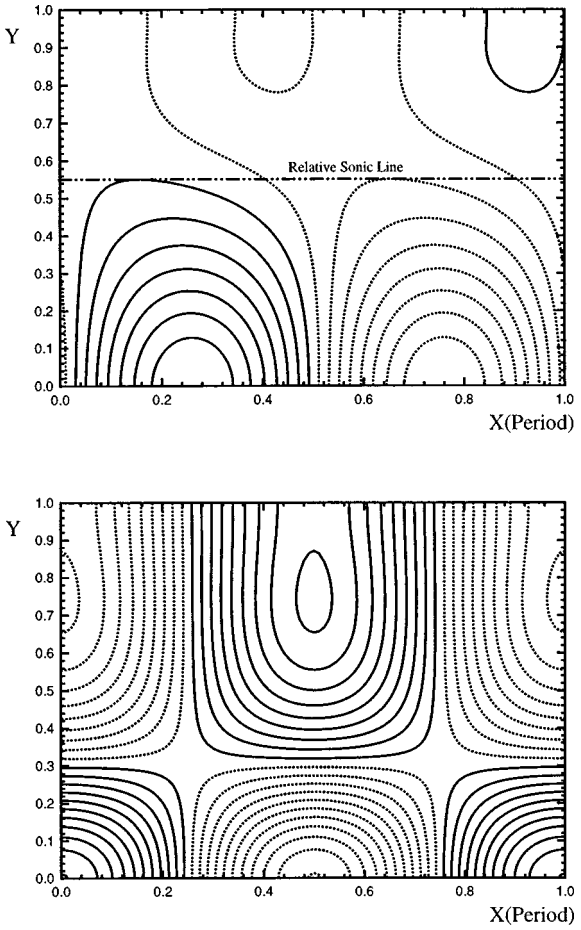

FIG. 12. The contours of the pressure perturbations for the odd acoustic modes (upper figure, mode I; lower figure, mode III) at $M_\infty=5$, $Re=5\times10^5$, and $\alpha=2.5$. Solid and dashed lines represent positive and negative perturbation levels, respectively.

C. Effects of viscosity

The effects of viscosity on the stability of supersonic Couette flow at both Mach 2 and 5 were investigated by comparing the viscous stability results with the inviscid results by Duck *et al.*[29] The focus was on the acoustic modes I and II because they are the most unstable modes in viscous supersonic Couette flow.

Figure 13 shows $\mathrm{Re}\{c\}$ of modes I and II as a function of α for $M_\infty=2$ at $Re=10^5$ and 10^6. The results of Duck *et al.* for these two modes at the inviscid limit are plotted in the same figure for comparison. The figure shows that the viscous wave speeds are almost the same as the inviscid results obtained by Duck *et al.* and are independent of the Reynolds numbers except when α is very small. Viscosity does not have a strong effect on the speeds of the wave modes. The figure also shows that, as α increases, $\mathrm{Re}\{c\}$ increases for mode II and decreases for mode I. The two modes cross the lines of $\mathrm{Re}\{c\}=1$ or 0 at α about 3.4. At α larger than 3.4, inviscid theory predicts that the two modes are no longer neutrally stable.

Figure 14 shows $\mathrm{Im}\{c\}$ of modes I and II as a function of α for $M_\infty=2$ at several Reynolds numbers. In the inviscid limit, mode I becomes stable with finite damping when $\mathrm{Re}\{c\}<1$, but mode II becomes unstable when $\mathrm{Re}\{c\}>0$. For mode I, the figure shows that at $Re=10^5$, the viscous results are very stable for the whole range of α. Unlike the inviscid results, there is an additional peak in the $\mathrm{Im}\{c\}$ distribution of the viscous results. As the Reynolds number increases, most part of viscous mode I approaches the inviscid limit from below the inviscid result. However, the peak of $\mathrm{Im}\{c\}$ in the viscous curves become more unstable than the inviscid solution. In fact, mode I becomes unstable in the case of $Re=5\times10^6$ for α near 3.7 at the peak. This figure and later figures in this paper show clearly that viscosity destabilizes the flow at certain combination of the Reynolds numbers and wavenumbers. Therefore, viscosity plays both stablizing and destabilizing roles for compressible Couette flow. As a result, there exists unstable mode I for viscous Couette flow at finite Reynolds numbers even though mode I is always stable or neutrally stable at the inviscid limit for this case. The figure also shows similar effects of viscosity on mode II as Reynolds numbers increase, even though the trend at large Reynolds numbers is not as clear because the Reynolds numbers used are not large enough due to the limit of numerical resolution. Again, there is a peak for the $\mathrm{Im}\{c\}$ curve of mode II. In the Reynolds numbers used in the calculations for Mach 2, there is no unstable viscous mode II.

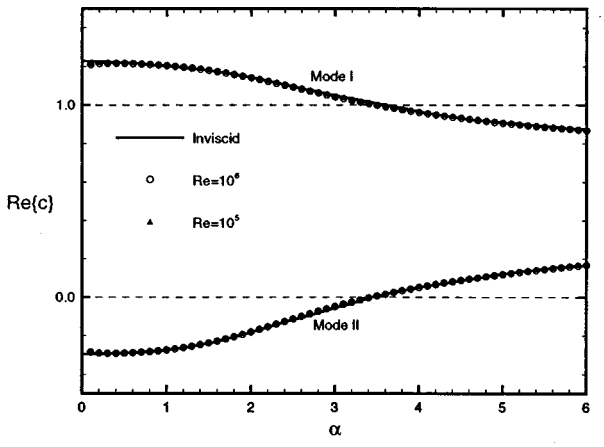

FIG. 13. Re$\{c\}$ of modes I and II as a function of α for $M_\infty=2$. The inviscid results of Duck *et al.* (1994) are compared with viscous results at $Re=10^5$ and $Re=10^6$.

As the Reynolds number increases, the figure shows that the growth rates corresponding to the second peaks increase for a fixed Mach number.

Similar viscosity effects on the stability of compressible Couette flow were also found at high Mach numbers. Figure 15 shows the real part and the imaginary part of the phase velocity of mode II as a function of wavenumber α at Mach 5 and three Reynolds numbers. Again, the results of Duck *et al.*[29] for inviscid mode II under the same flow condition are plotted in the figure for comparison. The figure shows that viscosity has little effect on the wave speed Re$\{c\}$. Except at very low α, the wave speed of mode II is almost independent of Reynolds numbers and agree very well with the inviscid results by Duck *et al.* On the other hand,

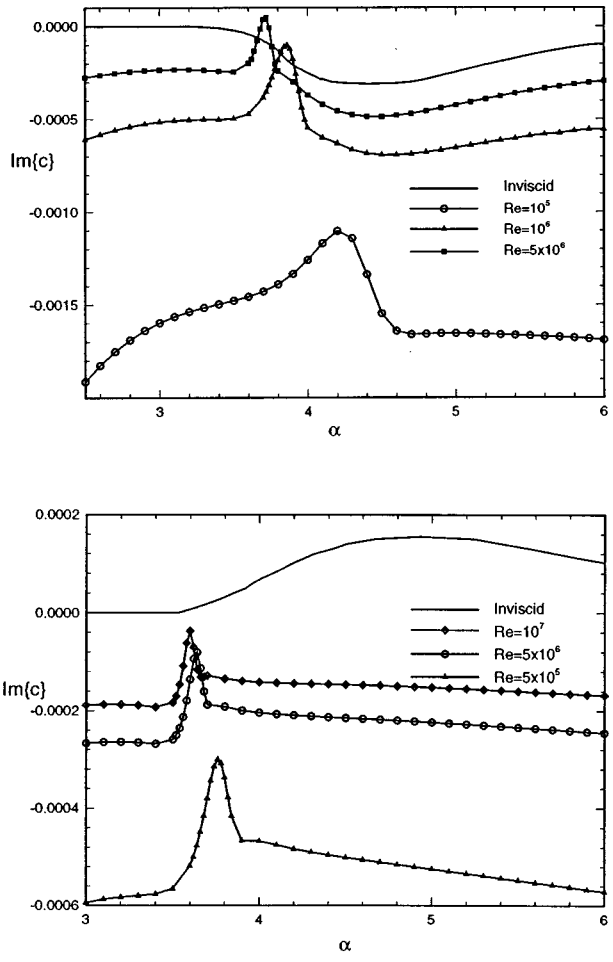

FIG. 14. Im$\{c\}$ of modes I and II as a function of α at $M_\infty=2$. The inviscid results of Duck *et al.* (1994) are compared with viscous results at different Reynolds numbers (upper figure, mode I; lower figure, mode II).

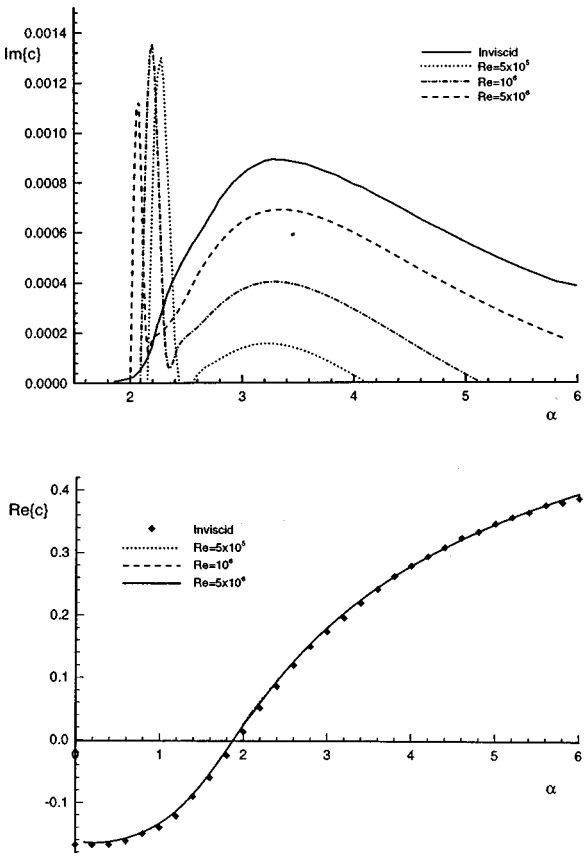

FIG. 15. Re$\{c\}$ and Im$\{c\}$ of mode II as a function of α at $M_\infty=5$. The inviscid results of Duck *et al.* (1994) are compared with viscous results at three Reynolds numbers.

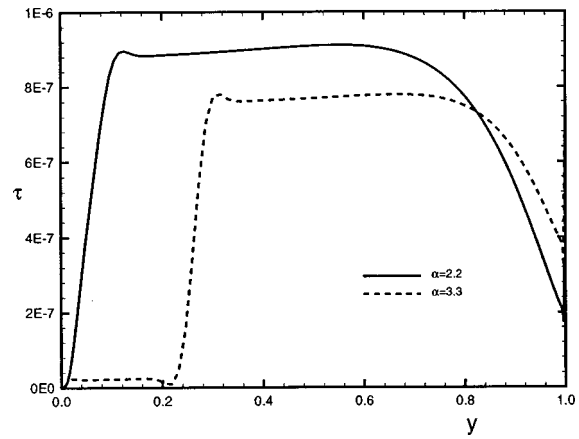

FIG. 16. The Reynolds stress ($\tau=\overline{\rho \mathrm{Re}\{u'\}\mathrm{Re}\{v'\}}$) profiles for mode II at $M_\infty=5$ and $Re=5\times10^6$.

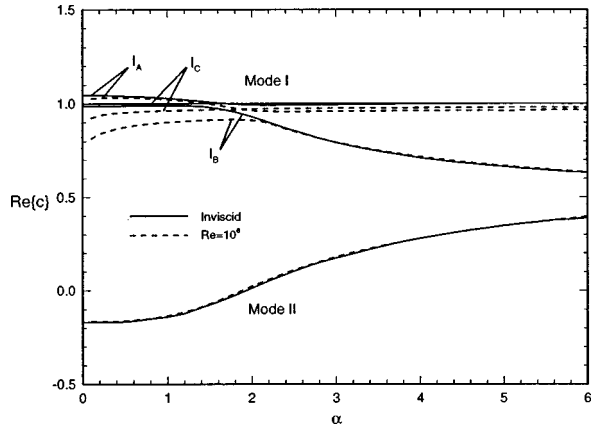

FIG. 17. Re$\{c\}$ of mode I and II as a function of α at $M_\infty=5$. The inviscid results (solid lines) of Duck *et al.* (1994) are compared with viscous results (dashed lines) at $Re=10^6$.

there are two peaks in the viscous Im$\{c\}$ curves for mode II comparing to one peak in the inviscid solutions. The first peak appears in a very narrow range of α between 2 and 2.5. The second peak appears at α around 3.3 in the figure, and it corresponds to the unstable solutions for the inviscid mode II. As the Reynolds number increases, most part of viscous mode II curves approaches the inviscid limit from below.

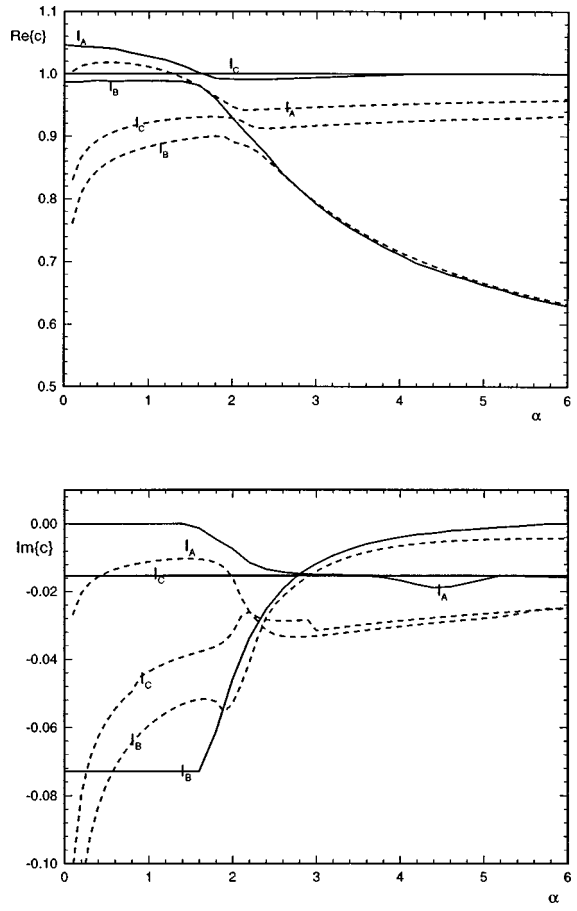

FIG. 18. Re$\{c\}$ and Im$\{c\}$ of mode I as a function of α at $M_\infty=5$. The inviscid results of Duck *et al.* (1994) shown in solid lines are compared with viscous results at $Re=10^5$ shown in dashed lines.

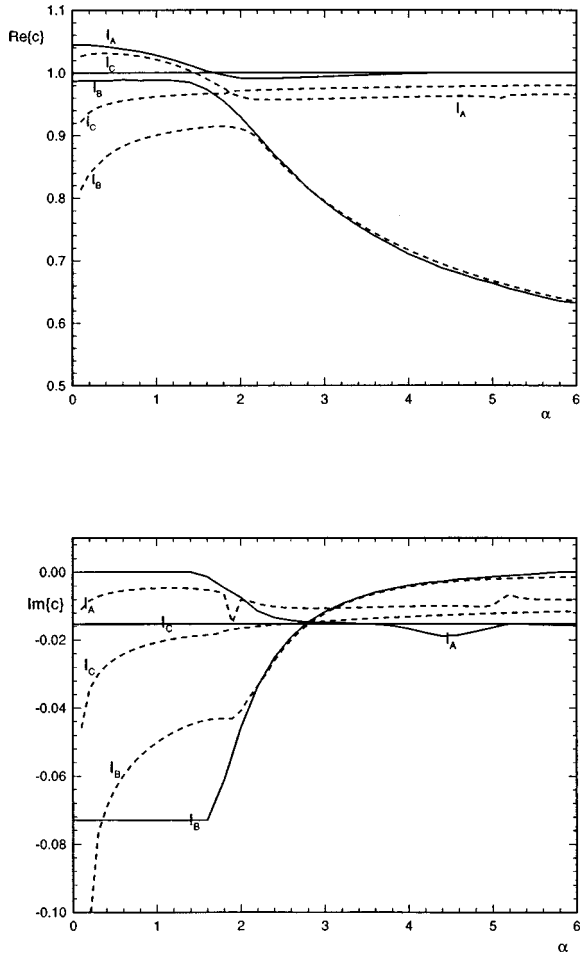

FIG. 19. Re$\{c\}$ and Im$\{c\}$ of mode I as a function of α at $M_\infty=5$. The inviscid results of Duck *et al.* (1994) shown in solid lines are compared with viscous results at $Re=10^6$ shown in dashed lines.

However, at the first peaks of the viscous curves, the flow become much more unstable than the flow in the inviscid limit. It will be shown in the next section along with the neutral stability contour results that this result is indeed viscous mode II instability in this small range of wavenumbers over a range of Reynolds numbers but the overall trend is that the viscous results match with the inviscid results as Reynolds number goes to infinity. In the inviscid limit, Duck *et al.*[29] showed that the upper family modes, such as mode II, change from neutrally stable to unstable when Re$\{c\}$ goes from negative to positive. The results of the viscous modes in Fig. 15 show a similar trend, though the viscosity effects delay the appearance of the unstable mode II.

The effects of viscosity on the viscous stability of supersonic Couette flow are further shown by Fig. 16 which shows the profile of Reynolds stress defined by

$$\tau=\overline{\rho \mathrm{Re}\{u'\}\mathrm{Re}\{v'\}}, \tag{48}$$

for mode II at $M_\infty=5$ and $Re=5\times10^6$ for two α's. The Reynolds stress for $\alpha=2.2$, which corresponds to the first peak in the Im$\{c\}$ distribution due to viscosity effects, is much larger than that for $\alpha=3.3$, which is close to the second peak (see Fig. 15). The figure indicates that viscosity

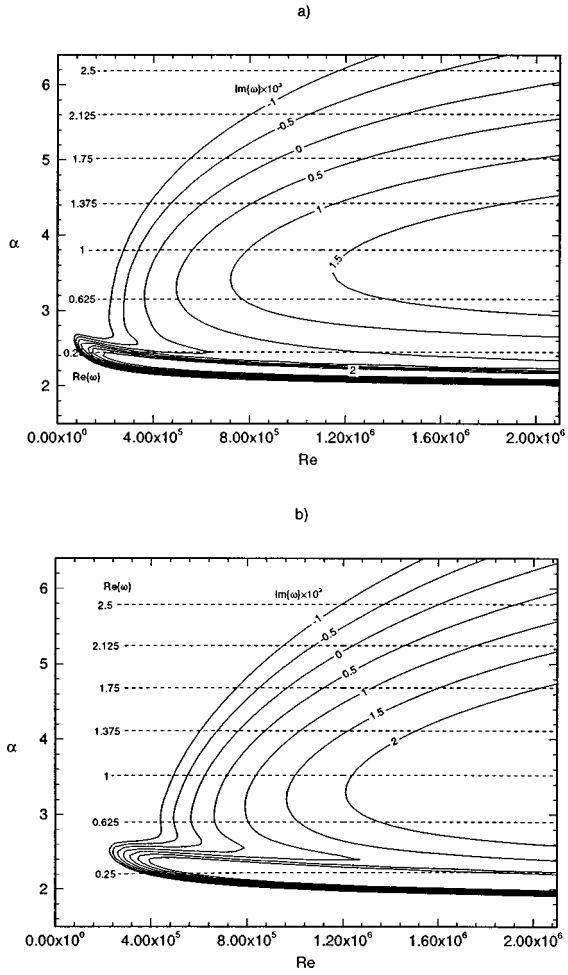

FIG. 20. The contours of frequency and growth rate for mode II as a function of wavenumbers and Reynolds numbers at (a) $M_\infty = 5$, (b) $M_\infty = 10$.

increases the Reynolds stress for α near the first peak and contributes to the destabilizing effects on the flow.

Figures 17 to 19 show $\mathrm{Re}\{c\}$ and $\mathrm{Im}\{c\}$ of mode I as a function of α for $M_\infty = 5$ at $Re = 10^5$ and $Re = 10^6$. Duck *et al.*[29] have shown that, at Mach 5, mode I breaks into three branches named I_A, I_B, and I_C. Consistent with the inviscid

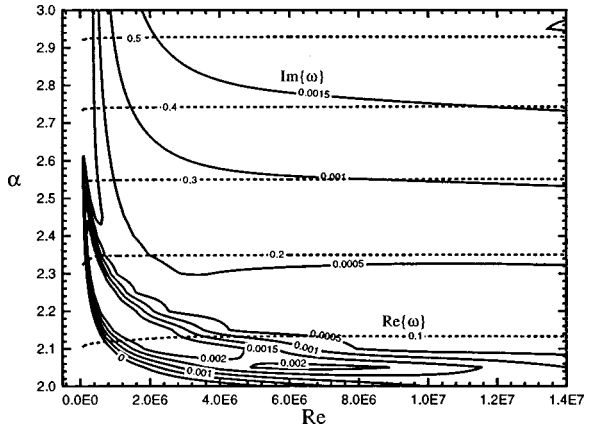

FIG. 21. The contours of frequency and growth rate of mode II at an extended Reynolds number range and a small wavenumber range near the first peak for the case of $M_\infty = 5.0$.

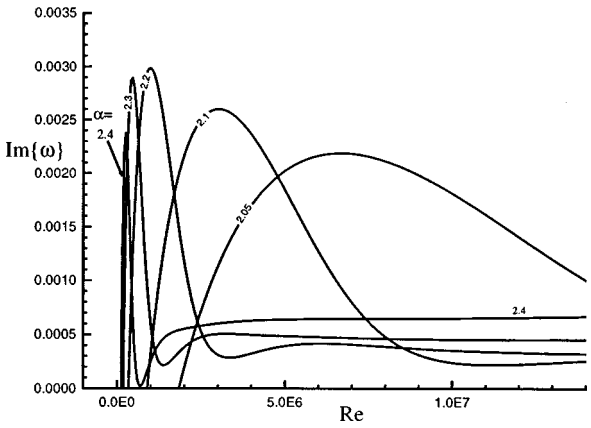

FIG. 22. The distribution of growth rates of mode II as a function of Reynolds numbers at fixed wavenumbers for the case of Mach 5.

results, there are three branches of mode I at Mach 5 and finite Reynolds numbers. The figures show that the wave speed of mode I is no longer independent of the Reynolds numbers. Again, the viscous results approach the inviscid results as Reynolds number increases.

D. Neutral stability contours

For practical applications, mode II is the most interesting mode because it dominates the instability of supersonic Couette flow. The neutral stability contours have been generated as functions of Reynolds numbers and wavenumbers. The contours of temporal amplification rates ($\mathrm{Im}\{\omega\}$) of mode II, including the neutral stability curves, at Mach 5 and Mach 10 along with the constant frequency curves are shown in Fig. 20. In the figure, the neutral stability curves correspond to the lines with $\mathrm{Im}\{\omega\} = 0$. The critical Reynolds numbers are approximately 90,000 and 260,000 for Mach 5 and Mach 10, respectively. Figure 20 shows that as Reynolds number increases, the range of the wavenumbers corresponding to the unstable region expands. Figures 20 and 15 both indicate that there are two peaks in the $\mathrm{Im}\{\omega\}$ curves. For the case of Mach 5, the narrow peak is located at $\alpha \approx 2.5$ and the wide peak is located at $\alpha \approx 3.5$. It is found that the narrow peak at smaller α is due to viscous instability while the wide peak at larger α is due to inviscid instability for acoustic wave modes. The viscous instability is shown in Fig. 15. The second peak with high α approaches the inviscid solutions as Reynolds number increases, while the first peak is unique to the viscous solutions. Figure 15 shows that as the Reynolds number increases, the first peak increases first. However, as the Reynolds number increases further, the amplification rate corresponding to the first peak reaches a maximum and decreases afterward, which is a result of viscous instability.

The destablizing effect of viscosity on the acoustic mode II can be demonstrated further by the frequency and growth rate contours at higher Reynolds numbers. Figure 21 shows the frequency and growth rate contours for a small range of wavenumbers near the first peak and a longer range of Reynolds numbers (comparing with Fig. 20). It is clear that at the first peak, the $\mathrm{Im}\{\omega\} = 0.002$ and $\mathrm{Im}\{\omega\} = 0.0015$ contour lines form closed curves at finite Reynolds numbers. This is

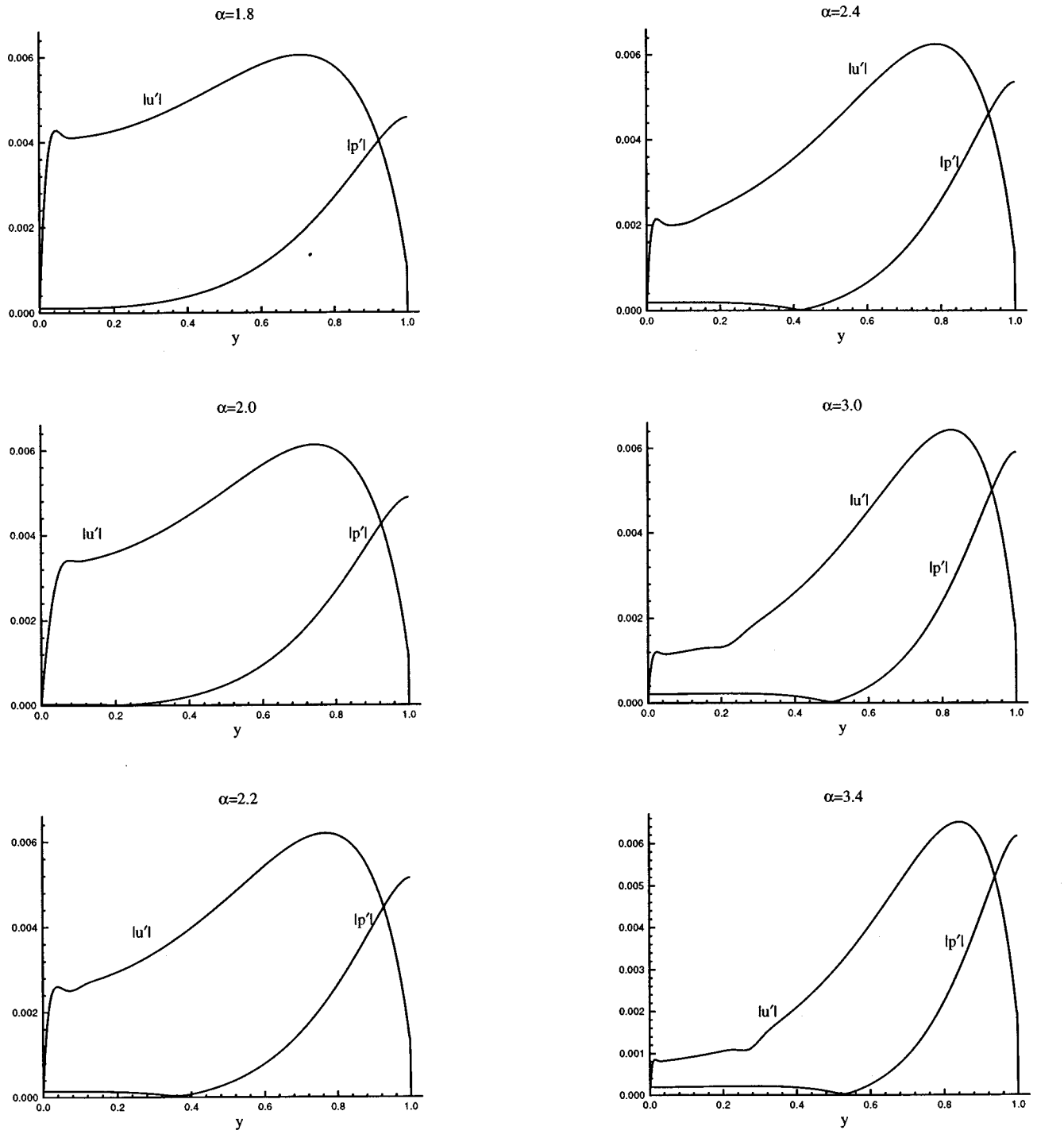

FIG. 23. The amplitude of $\hat{p}$ and $\hat{u}$ eigenfunctions corresponding to the $Re=10^6$ curve in Fig. 15 at different wavenumbers for $M_\infty=5.0$.

an indication of viscous instability. Figure 22 shows the distribution of growth rates as a function of Reynolds numbers of fixed wavenumbers at Mach 5. It also indicates that the low wavenumber peak would vanish and approach the inviscid results as the Reynolds number increases. Again, the narrow peak at smaller α is due to viscous instability while the wide peak at larger α is due to inviscid instability for acoustic wave modes. Similar results exist for the case of higher Mach number at $M_\infty=10$.

The viscous instability for the acoustic mode II for supersonic Couette flow is unexpected. In order to see if the two peaks indeed correspond to the same mode II, the amplitude of the eigenfunctions $\hat{p}$ and $\hat{u}$ of the mode at various wavenumbers are plotted in Fig. 23 corresponding to the $Re=10^6$ and Mach 5 curve in Fig. 15. It can be seen that the eigenfunctions at different α's are consistent, especially for $\hat{p}$. Along with the fact that the Re$\{c\}$ curves are smooth, the consistent eigenfunctions indicate that the two peaks indeed correspond to the same mode II. Figures 8, 9, and 10 show the mode II in the phase velocity spectra for the case of $M_\infty=5$ and $Re=5\times10^5$ for three wavenumbers in Fig. 15.

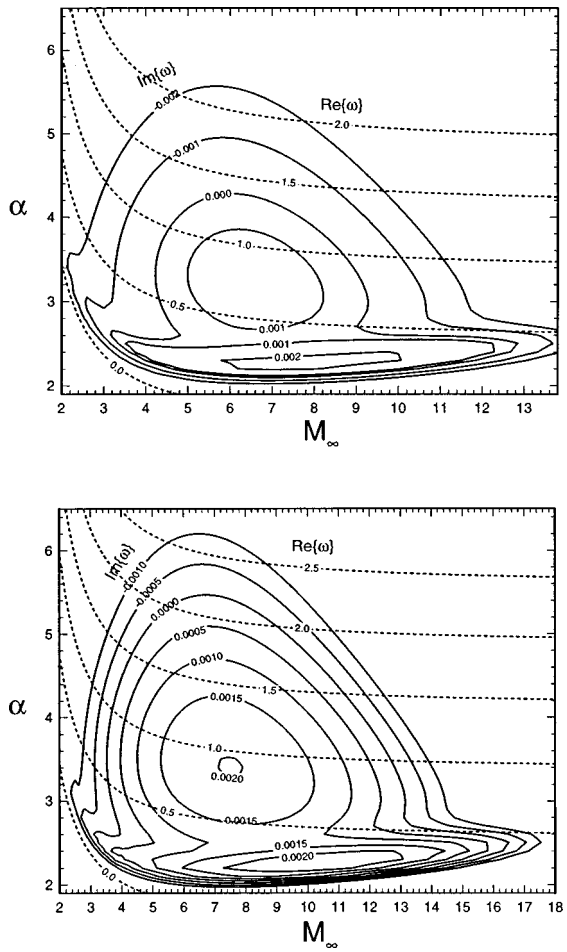

FIG. 24. The contours of complex frequency for mode II as a function of α and M_∞ (upper figure, $Re=5\times10^5$; lower figure, $Re=10^6$).

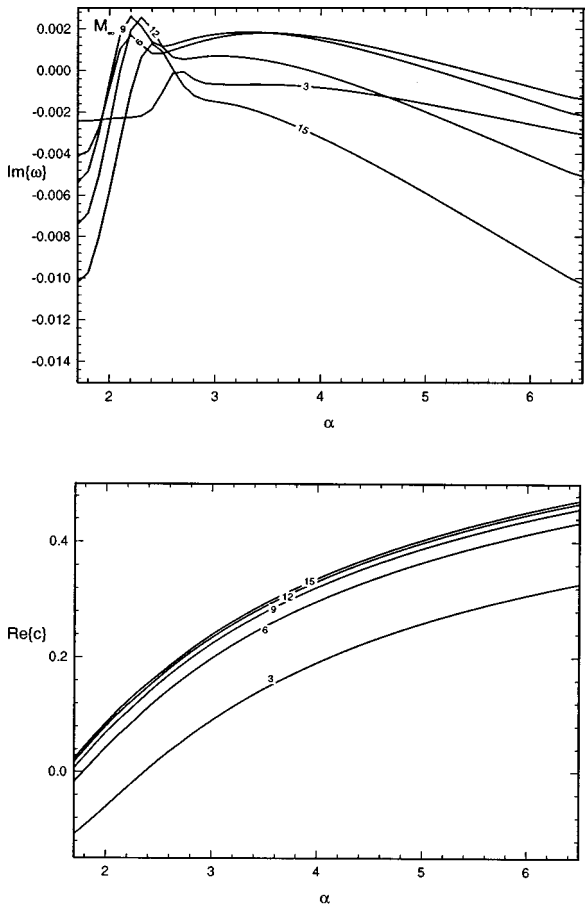

FIG. 25. Mode II phase velocity (upper figure) and amplification rate (lower figure) as a function of α at different Mach numbers for the case of $Re=5\times10^5$.

Three wavenumbers correspond to three cases of different α in the mode II curve in the first peak, the second peak, and outside of the second peak respectively. The figures show that at these three wavenumbers, mode II is clearly distinctive from other modes, which also confirms that they belong the same mode.

E. Effects of Mach number

For the effects of Mach number on mode II instability, Fig. 24 shows the contours of Re$\{\omega\}$ and Im$\{\omega\}$ for the most unstable mode II for a range of Mach numbers and wavenumbers while fixing Reynolds number at 5×10^5 and 10^6. In both cases, the unstable range for α expands first and then shrinks as Mach number increases. The figure shows that, for a fixed Reynolds number, there is a Mach number which corresponds to the maximum amplification rate for mode II. For Reynolds number at 5×10^5 and 10^6, the most unstable Mach number is around 8, 10, respectively. Therefore, for a fixed Reynolds number, as the Mach number increases, the flow will become more unstable first and become less unstable. The Mach number corresponding to the maximum amplification rate increases as the Reynolds number increases. Again, there are two peaks in the amplification rate contours of mode II. The long narrow peaks at smaller α are due to viscous instability while the wide peaks at larger α are due to inviscid instability for acoustic wave modes. The figures show that the viscous instability is stronger than its inviscid counterpart.

Figure 25 shows mode II phase velocity and amplification rate at $Re=5\times10^5$ as a function of α for various Mach numbers. The figure shows that Re$\{c\}$ of mode II reaches a finite limit as Mach number increases. For a fixed Reynolds number at $Re=5\times10^5$, as Mach number increases, the maximum Im$\{\omega\}$ first increases, reaches a maximum at certain Mach number, and then decreases. The Mach number corresponding to the maximum Im$\{\omega\}$ at $Re=5\times10^5$ is about 8. For the $Re=10^6$ case, the Mach number is close to 10. Notice that this Mach number is around 40 in the inviscid limit as shown in Fig. 12 of Ref. 29. Therefore, as Reynolds number increases, the most unstable Mach number for the second mode instability also increases, but has a finite limit.

Comparing Fig. 13 with Fig. 17, it is observed that mode I has three branches at $M_\infty=5$, but not at $M_\infty=2$. In addition, there is a prominent low α peak in Im$\{c\}$ at Mach 2 (Fig. 14) but not Mach 5 (Fig. 18). Both the present viscous results and the inviscid results of Duck *et al.* show similar trends. The reason for having three branches of mode I at Mach 5 is currently not known. One possible reason is that the three eigenmodes, I_A, I_B, I_C whose Re$\{c\}$ are close to 1,

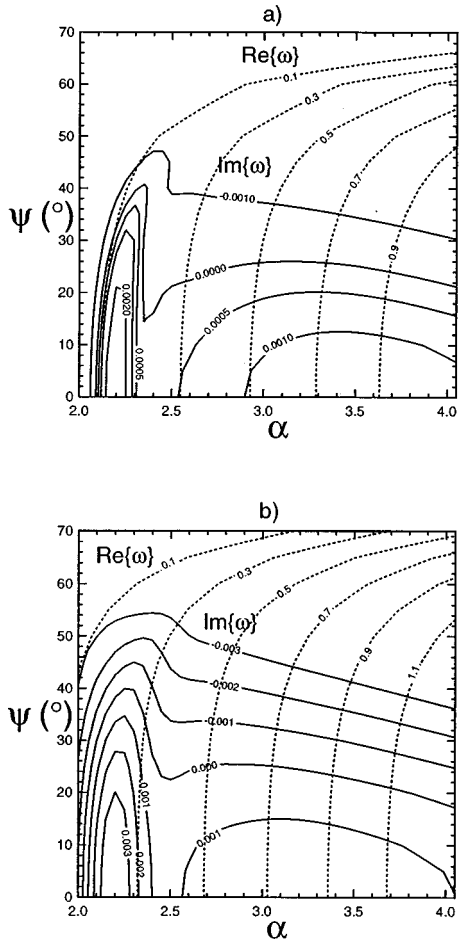

FIG. 26. Contours of frequency and amplification rate for mode II at $Re=10^6$ as a function of oblique wave angle ψ and α for (a) $M_\infty=5$, (b) $M_\infty=10$.

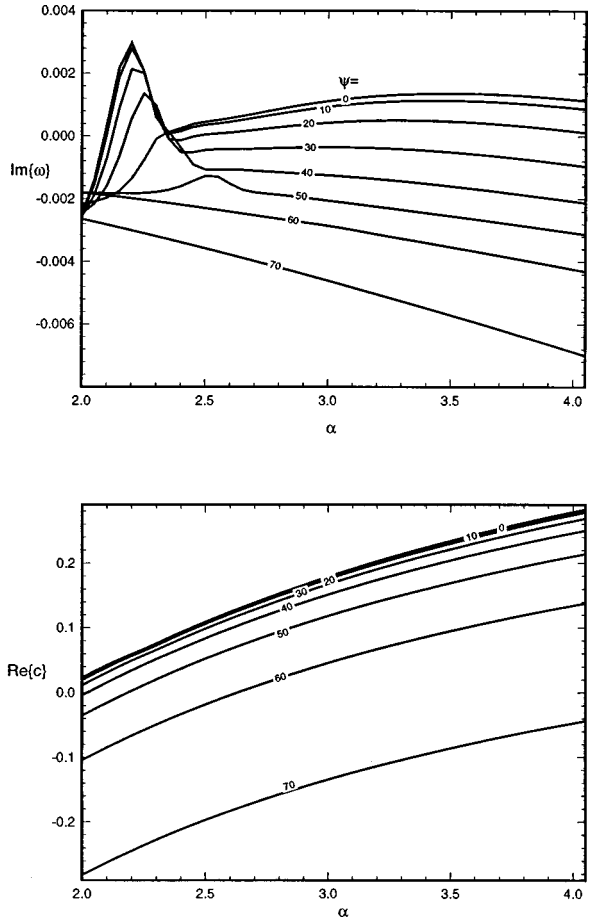

FIG. 27. Amplification rate and phase velocity of mode II at different oblique wave angles for $Re=10^6$ and $M_\infty=5$.

start to interact when their Re$\{c\}$'s get close to each other. As one can see from the inviscid and viscous results shown in the lower part of Fig. 16, the low α range I_A and the high α range I_B still resemble the mode I curve at Mach 2 except that the curve is ''broken'' in the middle due to the mode interactions. The interactions among eigenmodes are not observed at Mach 2. Furthermore, the narrow peak of Im$\{c\}$ for mode I is consistent with the narrow unstable region observed at M_∞ from 2.2 to 2.9 at $Re=10^6$ as shown in Fig. 29.

F. Three-dimensional wave modes

The effects of oblique wave angle on the stability of the most unstable mode II were next investigated by considering three-dimensional oblique disturbance waves with wave angle ψ defined by

$$\psi=\tan^{-1}(\beta/\alpha). \tag{49}$$

Figure 26 shows the complex frequency contours as a function of wavenumber α and wave angle ψ at Mach 5 and Mach 10, respectively. The Reynolds number is 10^6. The figure shows that as wave angle ψ increases for a fixed wavenumber α, both Im$\{\omega\}$ and Re$\{\omega\}$ decreases in general. Therefore, mode II is most unstable when it is two-dimensional. The effects of three dimensionality on the instability of mode II are similar to that of second mode in supersonic boundary layers.[4]

Figures 27 and 28 show the phase velocity and amplification rate of mode II as a function of wavenumber α for different wave angles ψ at Mach 5 and Mach 10, respectively. Again, three-dimensional waves are generally more stable then two-dimensional waves with an exception shown in Fig. 27 where there is a small range of α in which three-dimensional waves with wave angles around 30° are more unstable than the two-dimensional waves. This phenomenon, however, is not observed in the case of Mach 10.

G. Instability of mode I

Duck *et al.*[29] showed that the lower family of modes, such as mode I, are neutrally stable when Re$\{c\}\geqslant 1$ and become stable with finite damping when Re$\{c\}<1$. For viscous stability at finite Reynolds numbers, mode I was found to be unstable for a small range of Mach numbers. At $Re=10^6$, mode I instability is found to exist for a range of Mach numbers as shown in Fig. 29. The Im$\{\omega\}$ contours in the figure indicate that there is a narrow range Mach numbers and wavenumbers where mode I is unstable at this Reynolds number. As discussed earlier in the paper, this instability is caused by the effects of viscosity. In order to compare modes

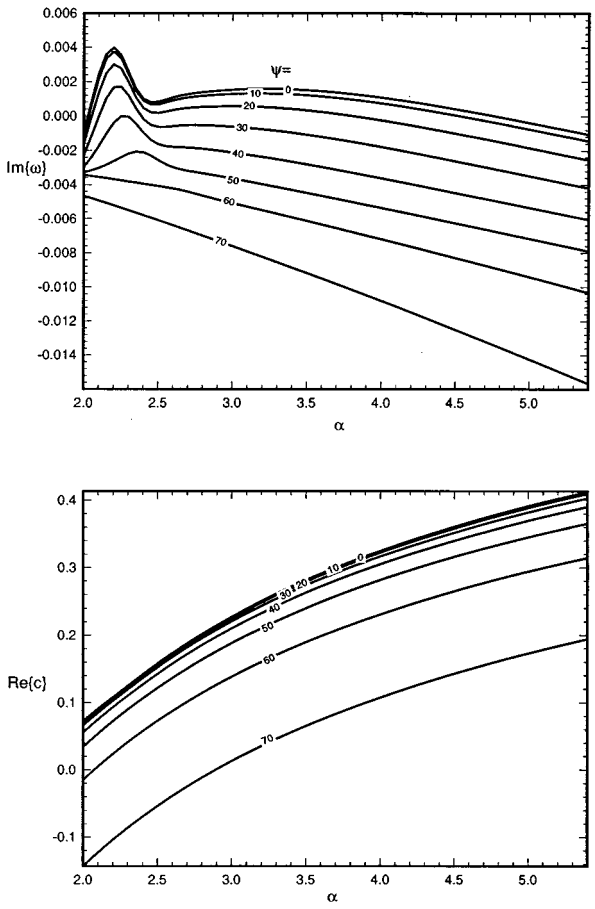

FIG. 28. Amplification rate and phase velocity of mode II at different oblique wave angles for $Re=10^6$ and $M_\infty=10$.

I and II instability, Fig. 30 shows the maximum amplification rates over a range of wavenumbers for a range of Mach numbers corresponding to mode I and mode II at $Re=10^6$. The symbols are the numerical data while the smooth curves are the polynomial fit results. The figure shows that mode I instability is much weaker than mode II instability. It only occurs in a very small range of Mach numbers. The nonsmoothness of the curves indicate that when Reynolds number is fixed, the maximum amplification rates for mode I and II are determined by combined effects of Mach number and wavenumber. The effects of Reynolds number on the mode I instability are illustrated in Fig. 31 for $M_\infty=2.9$ and $\alpha=2.5$. The results show that viscosity enhances the instability of mode I in certain range of Reynolds numbers. Figure 32 shows the effects of wave angle for mode I at $M_\infty=2.9$ and $Re=10^6$ as a function of α. When the wavenumber α is fixed, both Im$\{\omega\}$ and Re$\{\omega\}$ in general increase as wave angle ψ increases.

H. Effects of lower-wall cooling

The results presented so far are for the case of adiabatic condition at the lower wall and isothermal condition at the upper wall. The effects of lower-wall cooling on modes I and II instability for supersonic Couette flow are also investigated. Figure 33 shows the maximum Im$\{\omega\}$ (corresponding

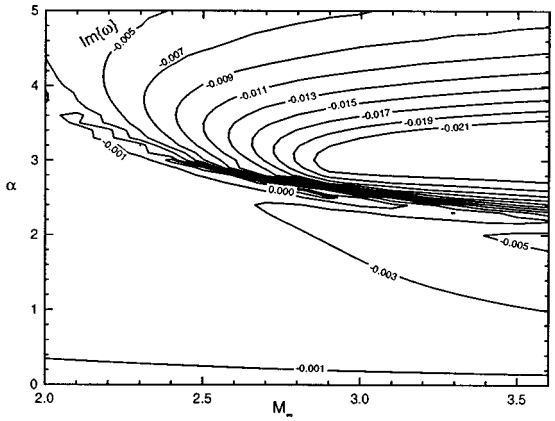

FIG. 29. Amplification rate contours for mode I at $Re=10^6$ as a function of α and M_∞.

to a range of wavenumbers) of the two-dimensional mode I for $M_\infty=2.5$ and $Re=10^6$ as a function of the ratio of the lower wall temperature and the lower wall recovery temperature given by Eq. (9). As the temperature of the lower wall decreases, mode I is first destabilized, then stabilized as the lower wall is further cooled. The effects of wall cooling on mode II are shown in Fig. 34 for $M_\infty=5$ and $Re=5\times10^5$. Similarly, mode II is first destabilized and then strongly stabilized as T_w decreases. The effects of wall cooling on the stability of modes I and II are different from those of the supersonic boundary layers, where Mack[4] showed that the second modes in the boundary layers are destabilized by wall cooling. The response of Couette flow modes I and II to wall cooling is different from that of compressible boundary layer because of the effects of additional upper wall in the bounded Couette flow.

V. CONCLUSIONS

The characteristics of linear viscous stability of supersonic plane Couette flow have been investigated numerically. The effects of viscosity on the stability of modes I and II were studied by comparing the viscous results at finite Rey-

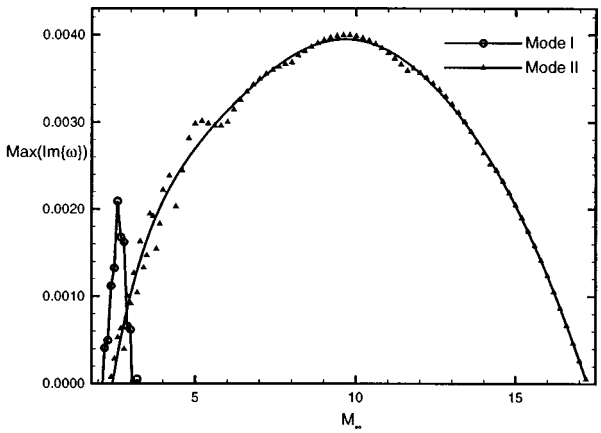

FIG. 30. Maximum Im$\{\omega\}$ of modes I and II for different Mach numbers at $Re=10^6$. The symbols are the numerical data. The smooth curves are polynomial fit results.

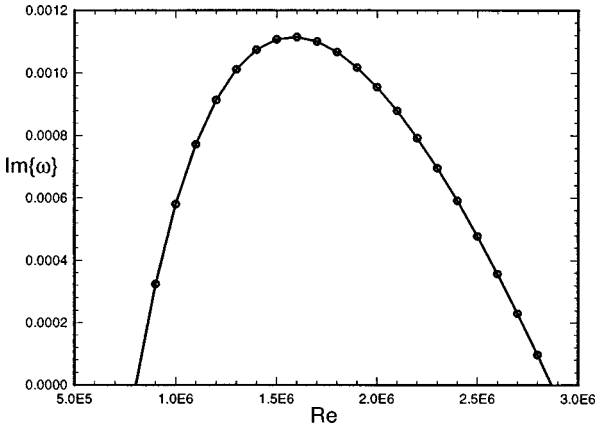

FIG. 31. The effects of Reynolds number on mode I instability at $M_\infty = 2.9$ and $\alpha = 2.5$.

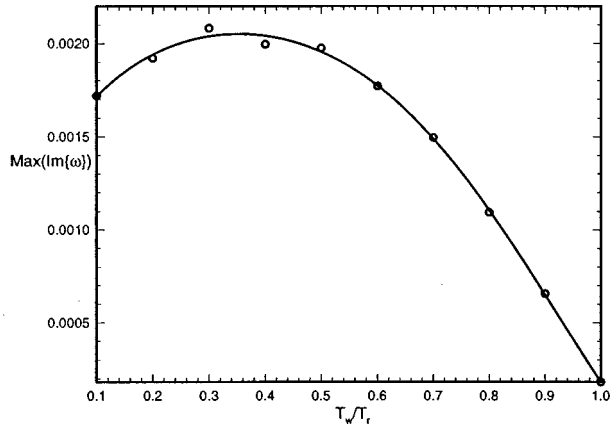

FIG. 33. The effects of wall-cooling on Im$\{\omega\}$ for mode I at $M_\infty = 2.5$ and $Re = 10^6$.

nolds numbers with the inviscid results of Duck *et al.* In addition, the effects of compressibility, three-dimensionality, and wall cooling on the two wave families were also studied. It was shown that viscosity plays a destabilizing role in both mode I and mode II stability for supersonic Couette flow in a range of Reynolds numbers and wavenumbers. Both of these modes are acoustic modes originated from the wave reflections in a supersonic region near the upper or lower wall. Viscosity stablizes the wave modes in most regions, but it destabilizes the wave modes in a narrow region of the Reynolds numbers and wavenumbers. Unlike the results at the inviscid limit that mode I is either stable with finite damping or neutrally stable, mode I is found to be unstable at finite Reynolds numbers due to the destabilizing effects of viscosity. The viscous results for mode II, on the other hand, are the dominant instability and unstable for a large range of Mach numbers and wavenumbers. The results show that as Reynolds number increases, the wave speeds and amplification rates of modes I and II approach the inviscid limit results. The characteristics of mode II instability have been investigated in more details by generating their neutral stability contours. The critical Reynolds numbers for Mach 5 and Mach 10 plane Couette flow were found to be around 90,000 and 260,000, respectively. Mode I and II, in general, are most unstable when they are two-dimensional. As for the Mach number effects, mode II is destabilized first and then stabilized as Mach number increases. The range of Mach numbers which has mode II instability expands with Reynolds number but remains finite. When the lower wall temperature decreases, both mode I and mode II are destabilized first, but they are stabilized as *Tw* decreases further. In general, the stability of the bounded Couette flow is different

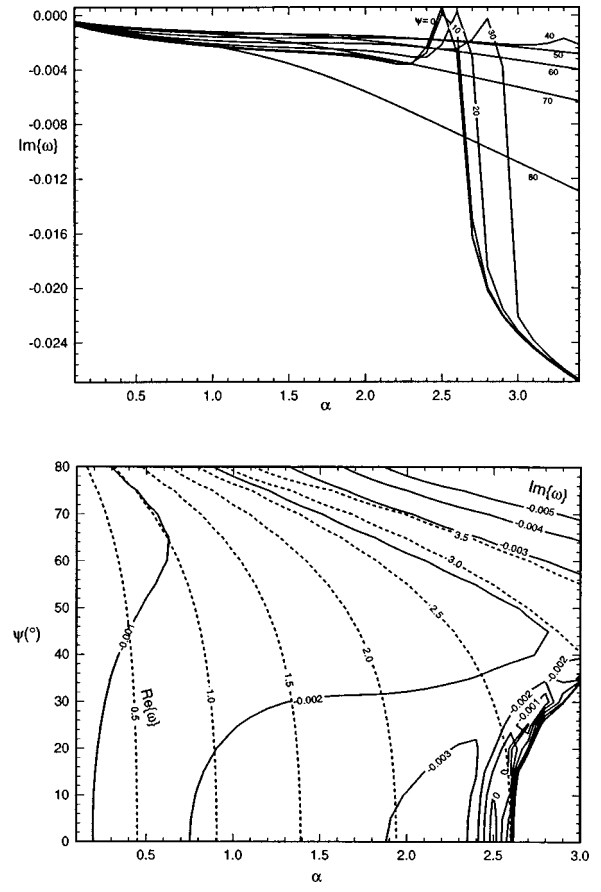

FIG. 32. Complex frequency of mode I as a function of wave angle ψ and wavenumber α at $M_\infty = 2.9$ and $Re = 10^6$: (a) upper figure, Im$\{\omega\}$ vs α at different oblique wave angles, (b) lower figure: contours of Im$\{\omega\}$ and Re$\{\omega\}$.

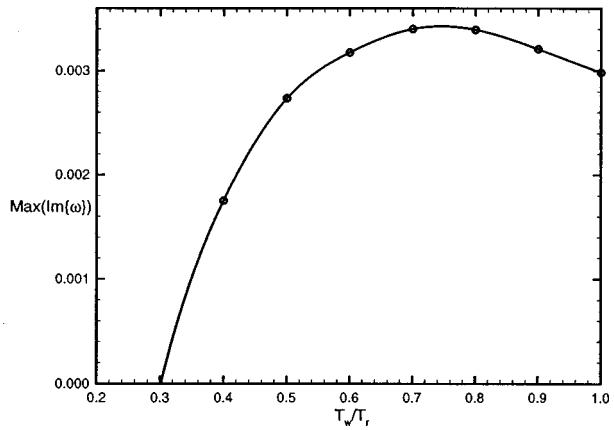

FIG. 34. The effects of wall-cooling on Im$\{\omega\}$ for mode II at $M_\infty = 5$ and $Re = 5 \times 10^5$.

from that of the unbounded supersonic boundary layers in many aspects due to the presence of the upper wall.

ACKNOWLEDGMENTS

This research was supported by the Air Force Office of Scientific Research under Grants Number F49620-94-1-0019 and F49620-95-1-0405 monitored by Dr. Len Sakell. The authors would like to thank Referee No. 1 for his insightful comments.

[1]L. Lees and C. C. Lin, ''Investigation of the stability of the laminar boundary layer in a compressible fluid,'' NACA Tech. Note 1115, 1993.
[2]L. M. Mack, ''Computation of the stability of the laminar compressible boundary layer,'' in *Methods in Computational Physics*, edited by B. Adler, S. Fernbach, and M. Rotenberg (Academic, New York, 1965), pp. 247–299.
[3]A. R. Wazzan, T. T. Okamura, and A. M. O. Smith, ''Spatial and temporal stability charts for the Falkner-Skan boundary-layer profles,'' McDonnell-Douglas Aircraft Co., Rep. No. DAC-67086, 1968.
[4]L. M. Mack, ''Boundary-layer linear stability theory,'' AGARD Rep. 704, 3–1, 1984.
[5]M. R. Malik and S. A. Orzag, ''Efficient computation of the stability of three-dimensional compressible boundary layers, AIAA paper No. 81-1277, 1981.
[6]L. M. Mack, ''Linear stability theory and the problem of supersonic boundary-layer transition,'' AIAA J. **13**, 278 (1975).
[7]L. M. Mack, ''Review of linear compressible stability theory,'' in *Stability of Time Dependent and Spatially Varying Flows*, edited by D. L. Dwoyer and M. Y. Hussaini (Springer, Berlin, 1987), pp. 164–187.
[8]L. M. Mack, ''On the inviscid acoustic-mode instability of supersonic shear flows, part 1: Two-dimensional waves,'' Theor. Comput. Fluid Dyn. **2**, 97 (1990).
[9]A. E. Gill, ''Instabilities of ''top-hat'' jets and wakes in compressible fluids,'' Phys. Fluids **8**, 1428 (1965).
[10]C. K. W. Tam and F. Q. Hu, ''On the three families of instability waves of high-speed jets,'' J. Fluid Mech. **201**, 447 (1989).
[11]M. G. Macaraeg and C. L. Street, ''New instability modes for bounded, free shear flows,'' Phys. Fluids A **1**, 1305 (1989).
[12]M. C. Macaraeg and C. L. Street, ''Linear stability of high-speed mixing layers,'' Appl. Numer. Math. **7**, 93 (1991).
[13]C. K. W. Tam and F. Q. Hu, ''The instability and acoustic wave modes of supersonic mixing layers inside a rectangular channel,'' J. Fluid Mech. **203**, 51 (1989).
[14]J. A. Greenough, J. J. Riley, M. Soetrisno, and D. S. Eberhardt, ''The effects of walls on a compressible mixing layer,'' AIAA paper 89-0372, 1989.
[15]M. Zhuang, P. E. Dimotakis, and T. Kubota, ''The effect of wall on a spatially growing supersonic shear layer,'' Phys. Fluids A **2**, 599 (1990).
[16]P. G. Drazin and W. H. Reid, *Hydrodynamic Stability* (Cambridge University Press, London, 1981).
[17]L. A. Dikii, ''On the stability of plane-parallel Couette flow,'' J. Appl. Math. Mech. **29**, 1009 (1965).
[18]A. P. Gallagher and A. McD. Mercer, ''On the behavior of small disturbances in plane Couette flow,'' J. Fluid Mech. **13**, 91 (1962).
[19]J. W. Deardroff, ''On the stability of viscous plane Couette flow,'' J. Fluid Mech. **15**, 623 (1963).
[20]A. P. Gallagher and A. McD. Mercer, ''On the behaviour of small disturbances in plane Couette flow, part 2: The higher eigenvalues,'' J. Fluid Mech. **18**, 350 (1964).
[21]A. Davey, ''On the stability of plane Couette flow to infinitesimal disturbances,'' J. Fluid Mech. **57**, 369 (1973).
[22]A. P. Gallagher, ''On the behaviour of small disturbances in plane Couette flow, part 3: The phenomenon of mode-pairing,'' J. Fluid Mech. **65**, 29 (1974).
[23]V. A. Romanov, ''Stability of plane-parallel Couette flow,'' Funct. Anal. Appl. **7**, 137 (1973).
[24]G. I. Taylor, ''Fluid friction between rotating cylinder,'' Proc. R. Soc. London, Ser. A **157**, 546 (1989).
[25]J. M. Robertson, ''On turbulent plane-Couette flow,'' in Proceedings of the 6th Mid. Western Conference on Fluid Mechanics, University of Texas, p. 169 (1959).
[26]W. Glatzel, ''Sonic instability in supersonic shear flows,'' Mon. Not. R. Astron. Soc. **233**, 795 (1988).
[27]W. Glatzel, ''The linear stability of viscous compressible plane Couette flow,'' J. Fluid Mech. **202**, 515 (1989).
[28]J. J. Girard, ''Study of the staiblity of compressible Couette flow,'' Ph.D. dissertation, Washington State University, 1988.
[29]P. M. Duck, G. Erlebacher, and M. Y. Hussaini, ''On the linear stability of compressible plane Couette flow,'' J. Fluid Mech. **258**, 131 (1994).
[30]M. R. Malik, ''Numerical methods for hypersonic boundary layer stability,'' J. Comput. Phys. **86**, 76 (1990).
[31]X. Zhong, ''Direct numerical simulation of hypsersonic boundary layer transition over blunt leading edges, part I: A new numerical method and validation,'' AIAA paper 97-0755, 1997.
[32]H. W. Liepmann and A. Roshko, *Elements of Gas Dynamics* (California Institute of Technology, 1957).
[33]S. C. Reddy, P. J. Schmid, and D. S. Henningson, ''Pseudospectra of the Orr–Sommerfeld operator,'' SIAM (Soc. Ind. Appl. Math.) J. Appl. Math. **53**, 15 (1993).